Cell Reports

Article

An organotypic model of ductular reaction reveals a mevalonate-dependent vulnerability in reactive biliary cells

Graphical abstract

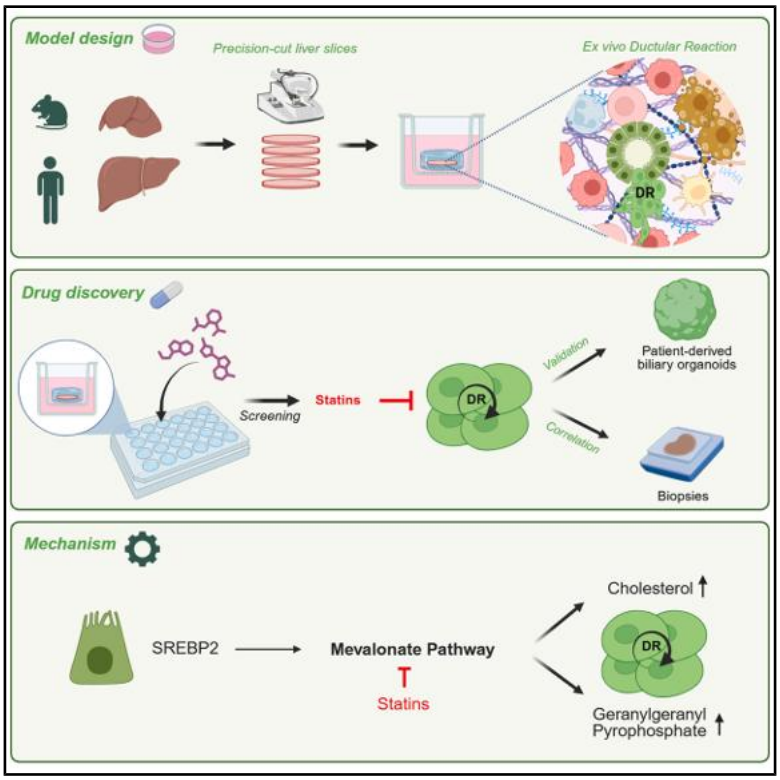

Highlights

- PCLS recapitulate ductular reaction within a native microenvironment
- Reactive biliary cells depend on the mevalonate pathway for proliferation
- Statins suppress ductular reaction in mouse and human liver models
- Statin therapy correlates with reduced ductular reaction in patient cohorts

Authors

Beatrice Anfuso, Suresh Velnati, Davide Selvestrel, ..., Guido Carpino, Fulvio Chiacchiera, Giovanni Sorrentino

Correspondence

giovanni.sorrentino@units.it

In brief

Chronic liver injury triggers the ductular reaction, where biliary cells expand to repair damage but can drive disease progression when persistent. Anfuso et al. model this process *ex vivo* within a native microenvironment using precision-cut liver slices and uncover a metabolic vulnerability targeted by statins in experimental systems and patients.

Anfuso et al., 2025, Cell Reports *44*, 116681
December 23, 2025
https://doi.org/10.1016/j.celrep.2025.116681

CellPress

Cell Reports

CellPress
OPEN ACCESS

Article

An organotypic model of ductular reaction reveals a mevalonate-dependent vulnerability in reactive biliary cells

Beatrice Anfuso,[1,15] Suresh Velnati,[1,15] Davide Selvestrel,[1,15] Clara Garlant,[1,11] Elisa Ferracci,[2] Gabriele Baj,[3] Pietro Parisse,[4,5] Diletta Overi,[6] Rebecca Bertolio,[1] Roberta Bulla,[3] Aurelio Sonzogni,[7] Matteo Bramuzzo,[8] Loredana Casalis,[4] Nicholas Cocomello,[9] Francesco Baratta,[9] Maria Del Ben,[9] Pablo Giraudi,[10] Claudio Tiribelli,[10] Natalia Rosso,[10] Manuela Mastronardi,[11,12] Paola Tarchi,[12] Maurizio Pinamonti,[13] Fabrizio Zanconati,[11] Nicolò de Manzini,[11,12] Eugenio Gaudio,[6] Silvia Palmisano,[11,12] Deborah Bonazza,[11] Giannino Del Sal,[1,3,14] Guido Carpino,[6] Fulvio Chiacchiera,[2] and Giovanni Sorrentino[1,11,16,*]

[1]International Centre for Genetic Engineering and Biotechnology (ICGEB), Area Science Park - Padriciano, 34149 Trieste, Italy
[2]Laboratory of Stem Cells and Cancer Genomics, Department of Cellular, Computational and Integrative Biology (CIBIO), University of Trento, Trento, Italy
[3]Department of Life Sciences, University of Trieste, Trieste, Italy
[4]Elettra-Sincrotrone Trieste, Area Science Park Basovizza, 34149 Trieste, Italy
[5]Institute of Materials (IOM), Italian National Research Council (CNR), Area Science Park Basovizza, 34149 Trieste, Italy
[6]Department of Anatomical, Histological, Forensic Medicine and Orthopaedic Sciences, Sapienza University of Rome, Roma, Italy
[7]Department of Pathology, Policlinico di Monza, Monza, Italy
[8]Institute for Maternal and Child Health - IRCCS "Burlo Garofolo," Trieste, Italy
[9]Department of Clinical Internal, Anesthesiologic and Cardiovascular Sciences, Sapienza University of Rome, Rome, Italy
[10]Fondazione Italiana Fegato, Area Science Park Basovizza, Trieste, Italy
[11]Department of Medical, Surgical and Health Sciences, University of Trieste, Trieste
[12]Surgical Clinic Unit, Cattinara Hospital, ASUGI, Strada di Fiume, 447, 34149 Trieste, Italy
[13]Department of Pathology, University Hospital Cattinara, Trieste, Italy
[14]IFOM ETS, The AIRC Institute of Molecular Oncology, Milan, Italy
[15]These authors contributed equally
[16]Lead contact
*Correspondence: giovanni.sorrentino@units.it
https://doi.org/10.1016/j.celrep.2025.116681

SUMMARY

Chronic liver injury is marked by the emergence of ductular reaction (DR), where reactive biliary epithelial cells (BECs) proliferate and engage in multicellular networks, driving disease progression. Despite its clinical relevance, the mechanisms underlying DR activation remain elusive, partly due to the lack of physiologically relevant models. Here, we developed an organotypic *ex vivo* model of DR using precision-cut liver slices (PCLS) from mouse and human tissue, which preserves native architecture and enables *de novo* activation of BECs. Through integrated analysis of PCLS and patient-derived organoids, we identified the mevalonate (MVA) pathway as a metabolic dependency of DR. Mechanistically, accumulation of cholesterol and geranylgeranyl-pyrophosphate is required to sustain a reactive BEC phenotype. Importantly, MVA pathway activation was confirmed in patient biopsies, and statin use suppressed DR both *ex vivo* and in clinical cohorts. These findings establish an innovative translational platform and reveal an actionable metabolic vulnerability in human DR cells.

INTRODUCTION

Ductular reaction (DR) is a stereotyped epithelial response to sustained liver injury, characterized by the emergence of reactive duct-like structures expanding from the portal region to reestablish biliary integrity and ensure bile drainage. Depending on the etiology and severity of liver injury, DR cells may also invade the hepatic lobule and ultimately differentiate into hepatocytes, thereby contributing to parenchymal regeneration in mice.[1] This adaptive regenerative process is coordinated by epithelial cells with biliary phenotype, including both bipotent hepatic progenitor cells and mature cholangiocytes (also known as biliary epithelial cells, BECs).[2,3] Moreover, recent evidence suggests that DR can also involve the plastic conversion of hepatocytes into cells with biliary features, particularly under conditions of chronic injury.[4] Although DR is initially triggered as a regenerative response, its functional contribution to liver repair remains unproven in humans. On the contrary, compelling experimental and clinical evidence indicates that, in chronic liver diseases, persistent DR correlates with worse clinical outcomes.[5] Over time, DR cells can adopt a pro-inflammatory and pro-fibrogenic phenotype, secreting cytokines and chemokines that recruit and

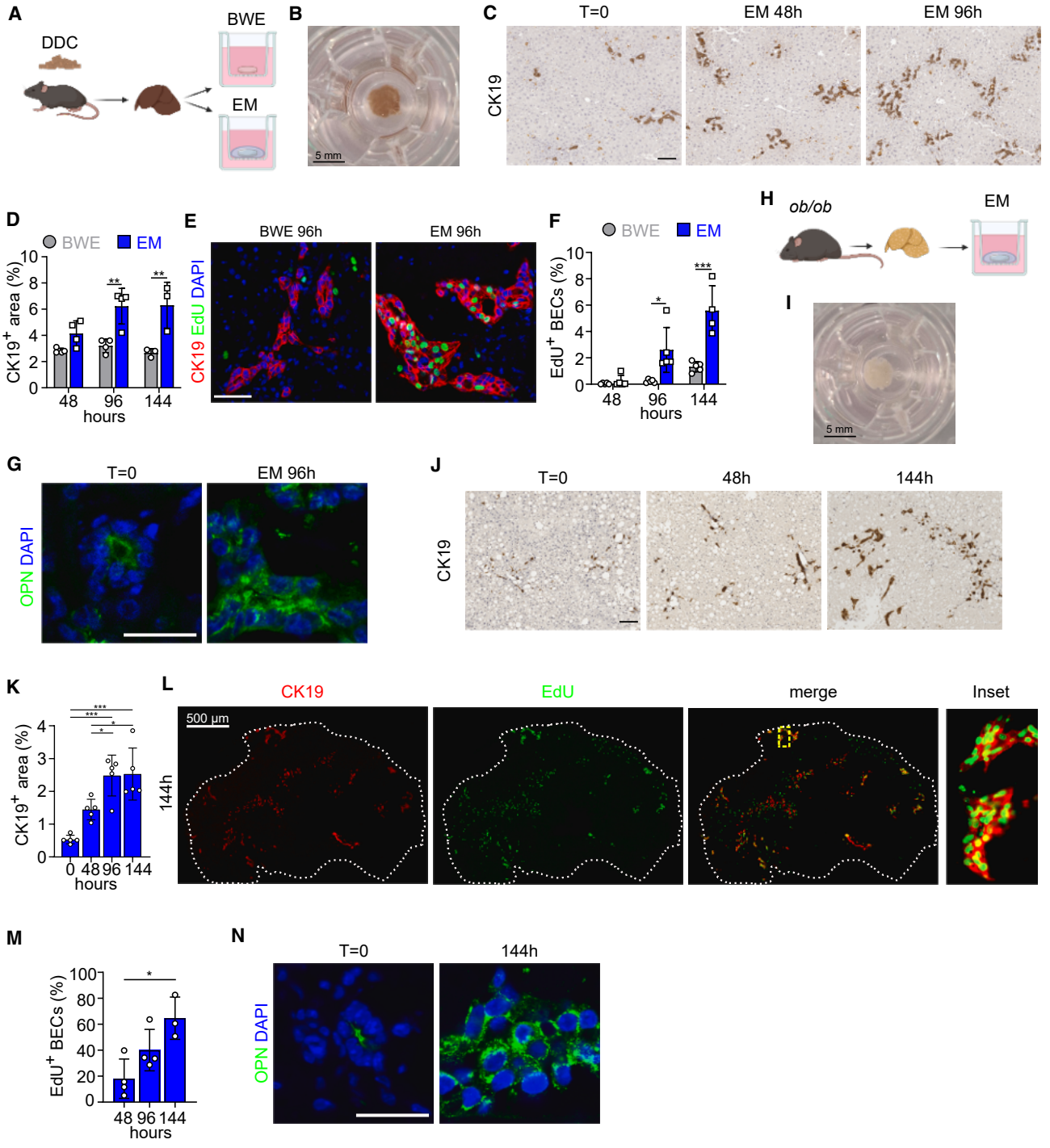

Figure 1. *Ex vivo* expansion of BECs in mouse PCLS

(A) Overview of PCLS establishment from mice fed DDC and the experimental setup.

(B) Representative appearance of PCLS. Scale bars, 5 mm.

(C) Representative immunohistochemical staining of CK19 in PCLS cultured in EM. Scale bars, 100 µm.

(D) CK19$^+$ area quantification in PCLS depicted in (C) (n = 3–4). A two-way ANOVA was used for statistical testing, column factor (medium) $p < 0.0001$, row factor (hours) $p = 0.058$. Tukey's post hoc test was used for multiple comparisons.

(E) Representative immunofluorescence staining of CK19 and EdU in PCLS. Scale bars, 50 µm.

(F) Quantification of CK19-EdU double-positive biliary cells in PCLS (n = 4–5). A two-way ANOVA was used for statistical testing, column factor (medium) $p < 0.0001$, row factor (hours) $p < 0.0001$. Tukey's post hoc test was used for multiple comparisons.

(legend continued on next page)

activate immune cells, sustain chronic inflammation, and stimulate hepatic stellate cells and portal fibroblasts, thereby promoting extracellular matrix (ECM) deposition and fibrogenesis.[6] Consistently, DR cell deletion reduces liver fibrosis in cholestatic injuries.[7] This phenomenon is observed in virtually all liver diseases, including cholangiopathies such as primary sclerosing cholangitis (PSC), alcoholic hepatitis, and advanced stages of metabolic dysfunction-associated steatotic liver disease (MASLD).[8] Consequently, targeting this maladaptive response has emerged as a promising therapeutic strategy to inhibit liver fibrosis progression and delay disease advancement.[5,7,9–14]

Despite growing interest, the molecular mechanisms governing the dynamic transition of progenitors and BECs from a quiescent to a reactive and proliferative state remain largely unknown. While different cell autonomous mechanisms have been characterized, more complex regulatory layers of DR control, involving the cross-talk of reactive BECs with their niche, are currently emerging.[15–18] Nevertheless, a major challenge in studying this complex pathological process lies in the absence of physiologically relevant culture models that faithfully recapitulate the intricate interactions between reactive BECs and their microenvironment.[19]

Precision-cut liver slices (PCLS) represent a sophisticated culture system consisting of thin liver tissue sections characterized by a reproducible and well-defined thickness, generated from freshly isolated tissues. PCLS offer a unique advantage over conventional 2D and 3D cultures as they retain the complex multicellular architecture of the hepatic microenvironment and its native geometric configuration, preserving essential cell-cell and cell-matrix interactions.[20]

In this study, we implemented the PCLS technology to establish an organotypic culture system that preserves—and even initiates de novo—a DR *ex vivo* within the intact native microenvironment, providing a physiologically relevant model to investigate the mechanisms governing biliary cell activation.

RESULTS

Development of a mouse PCLS platform to model DR *ex vivo*

In recent years, the application of PCLS has predominantly targeted hepatocyte metabolism, with limited attention given to biliary and progenitor cells. As a result, PCLS have traditionally been cultured as floating tissue slices in basal Williams E (BWE) medium, a condition that supports hepatocyte viability.[21] To model a DR response *ex vivo*, we implemented this established set-up by enriching the standard BWE medium with molecules that have been previously found to support the expansion of reactive BECs, containing niche factors (hereinafter referred to as expansion medium, EM).[22] Additionally, to provide physical support and to minimize the efflux of non-epithelial cells from the slices, we embedded PCLS in a basement membrane-like matrix.[23] To evaluate the effectiveness of this approach, we first tested whether our implemented culture system could maintain a pre-existing DR. To this aim, we first activated a DR *in vivo* by feeding mice a 3,5-diethoxycarbonyl-1,4-dihydrocollidine (DDC) diet for 3 weeks (Figures S1A and S1B). We then derived PCLS from these mice and cultured them either in BWE or EM, on *trans*-well inserts (Figures 1A and 1B). Remarkably, we found that biliary cells continued to expand *ex vivo* within PCLS cultured in EM, an effect not observed in BWE (Figures 1C, 1D, and S1C–S1E). The progressive expansion of the biliary cells over time was suggestive of a DR occurring within PCLS. To confirm this observation, we performed a 5-ethynyl-2′-deoxyuridine (EdU) assay in PCLS and monitored the proliferation of CK19$^+$ BECs *ex vivo*. Confirming our hypothesis, starting from 96 h in culture, we observed numerous CK19$^+$ proliferative cells within the slices (Figures 1E and 1F). Furthermore, we observed that osteopontin (Opn), typically restricted to the apical domain under homeostatic conditions, became diffusely localized within the cytoplasm of the expanding ductular structures—reflecting a transition toward a reactive and immature cellular state (Figure 1G).[24,25] PCLS maintained structural integrity of the parenchyma, with preservation of lobular arrangement and periportal fibrosis, and supported biliary cell proliferation for up to 10 days (Figures S1F and S1G). Finally, the assessment of hepatocyte senescence, necrosis, and proliferation in PCLS confirmed that DR arises in the same pathophysiological setting that drives biliary cell activation *in vivo*, characterized by parenchymal injury and defective hepatocyte regeneration[1] (Figures S1H–S1J). Based on this evidence, we concluded that the implemented PCLS cultures can efficiently maintain and propagate *ex vivo* and a DR initiated *in vivo*, over extended culture periods.

To evaluate whether the implemented PCLS platform could initiate a DR *de novo*, in the absence of overt pre-existing activation, we used leptin-deficient ob/ob mice—an early-stage MASLD model characterized by mild BEC reactivity and underlying hepatocellular stress (Figures 1H, 1I, S2A, and S2B). We reasoned that this background could prime the tissue to respond to niche-derived cues, thereby better recapitulating DR onset during the early stages of human liver disease.[26,27] As expected, PCLS did not show any clear evidence of an overt DR at the initial

(G) Representative immunofluorescence staining of Opn. Scale bars, 25 μm.
(H) Overview of PCLS establishment from ob/ob mice and experimental setup.
(I) Representative appearance of PCLS. Scale bars, 5 mm.
(J) Representative immunohistochemical staining of CK19 in PCLS. Scale bars, 100 μm.
(K) CK19$^+$ area quantification in PCLS depicted in (J) ($n = 5$). A one-way ANOVA was used for statistical testing, $p < 0.001$. Tukey's post hoc test was used for multiple comparisons.
(L) Representative immunofluorescence staining of CK19 and EdU in PCLS. Scale bars, 500 μm.
(M) Quantification of CK19-EdU double-positive biliary cells in PCLS ($n = 3$–4). A one-way ANOVA was used for statistical testing, $p < 0.05$. Tukeys's post hoc test was used for multiple comparisons.
(N) Representative immunofluorescence staining of Opn. Scale bars, 25 μm.
p value summary: $^*p < 0.05$, $^{**}p < 0.01$, and $^{***}p < 0.001$.

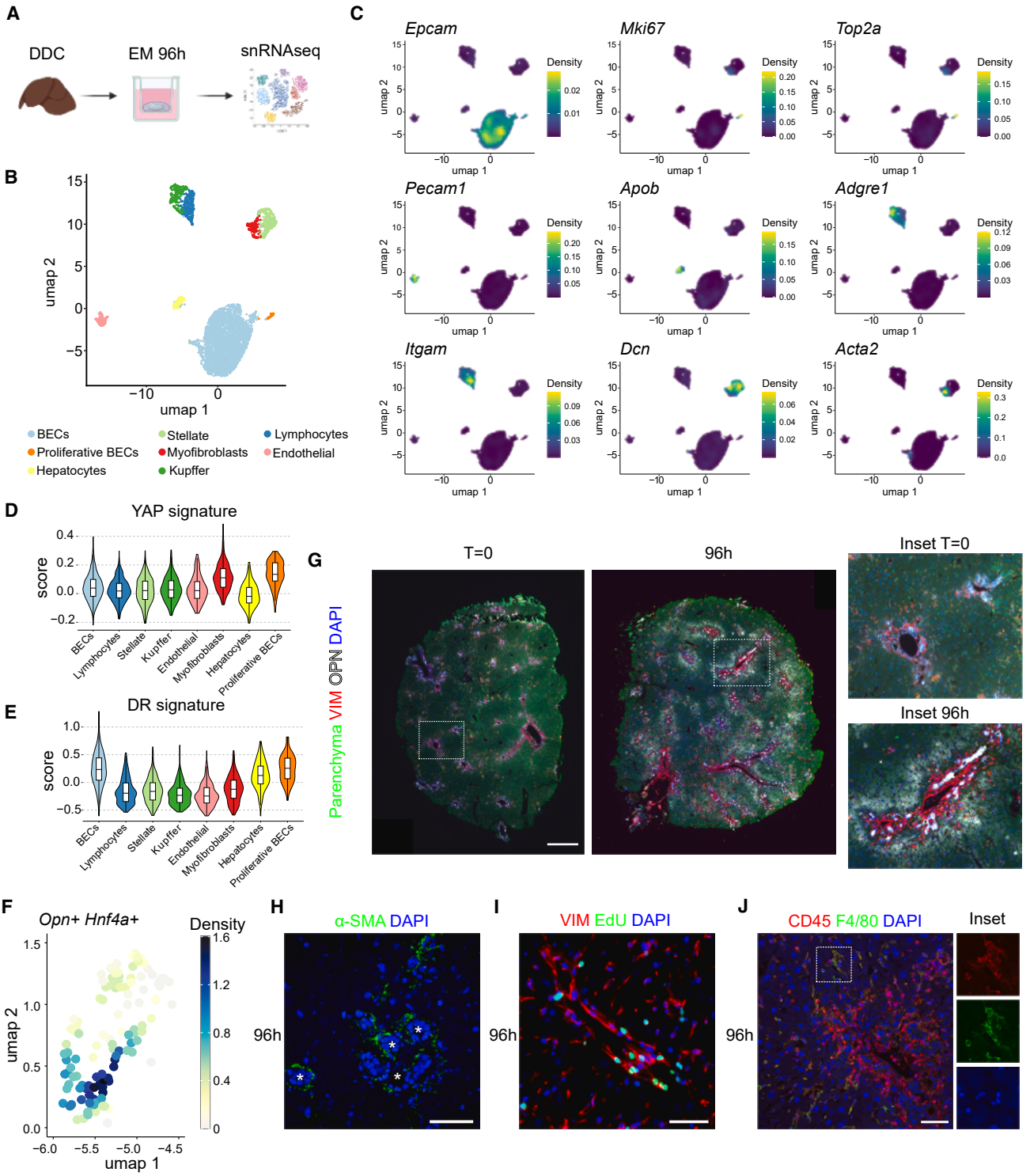

Figure 2. Cellular composition of the PCLS niche revealed by snRNA-seq and immunofluorescence

(A) PCLS obtained from DDC-fed mice were maintained in culture for 96 h and processed for snRNA-seq.

(B) UMAP projection showing cell annotation of single nuclei from mouse PCLS after quality control.

(C) Density plots displaying the expression of representative marker genes for each cluster identified in (B).

(legend continued on next page)

time point (Figure 1J). Strikingly, however, the supplemented culture medium supported a robust activation of the reactive BECs, resulting in the gradual emergence and expansion of CK19$^+$ proliferative cells that acquired an irregular, migratory-like morphology over time (Figures 1J–1N, S2C, and S2D). Moreover, we found that DR could also arise in PCLS from healthy wild-type mice cultured in EM, but not in BWE, and its emergence was temporally associated with reduced cell viability (Figures S2E–S2H). These data indicate that pre-injury is not strictly required for BEC activation in PCLS, as spontaneous parenchymal stress during *ex vivo* culture can trigger DR when appropriate niche factors are present.

In conclusion, this PCLS-based system proves capable of maintaining an active DR *ex vivo* in slices derived from DDC-fed mice, while also enabling the emergence of a DR, *de novo*, in slices from both obese and healthy mice.

Preservation of a native microenvironment supports physiologically relevant DR induction in PCLS

The DR depends on the coordinated participation of multiple microenvironmental components.[2] To ensure that the DR observed in our model truly reflects a physiologically relevant process, we characterized key microenvironmental components. As a first step, we evaluated whether the fibrosis-associated collagen deposited *in vivo* in DDC-fed mice was retained in PCLS *ex vivo*. To this aim, we performed quantitative analysis of collagen areas using Sirius red staining and confirmed that the portal fibrosis was stably maintained throughout the period of reactive BECs' activation (Figures S2I and S2J).[28] Next, we focused on the hepatic cell ecosystem.[11] To this aim, we performed a comprehensive PCLS profiling at single-cell resolution, using single-nucleus RNA sequencing (snRNA-seq) on slices derived from DDC-fed mice and cultured in EM for 96 h (Figure 2A). Of note, the analysis of 6,095 isolated nuclei (Figure S2K) and comparison with livers from wild-type mice fed either a DDC or a standard diet (Figures S2L and S2M) confirmed that the *ex vivo* cultured PCLS contain all expected cell types of the liver with a marked over-representation of biliary cells—an expected consequence of biliary cell expansion *ex vivo* and of the use of tissues derived from the DDC model. In particular, we identified 6 major cell-type-specific clusters, including BECs, hepatocytes, hepatic stellate cells (HSCs), Kupffer cells (KCs), lymphocytes, and endothelial cells (ECs) (Figures 2B, 2C, and S2K). Confirming the appearance of bona fide DR cells in the PCLS, the BECs population displayed a distinct cluster—which we termed "proliferative BECs"—characterized by the expression of proliferation markers and activation of the Hippo nuclear transducer YAP, a master regulator of DR[17] (Figures 2B–2D and S2N; Table S4). Furthermore, BECs within PCLS exhibited a strong expression of a small custom-designed DR signature (Table S4) (Figure 2E). To explore the dynamic transcriptional reprogramming of biliary epithelial cells into DR cells, we compared cholangiocytes from healthy livers, DDC-injured livers, and DDC-derived PCLS after 96 h (Figures S2O and S2P). Uniform manifold approximation and projection (UMAP) analysis revealed a continuum from quiescent to reactive and proliferative states, with PCLS-derived cells forming reactive clusters that included all DDC clusters and extended into regions enriched for DR and proliferation genes. (Figure S2Q). Next, we focused on hepatocytes and found that a subset of cells in this cluster showed a hybrid phenotype expressing genes normally restricted to the biliary lineage, such as *Opn* (Figure 2F). This evidence was reminiscent of a ductal *trans*-differentiation of hepatocytes, a histopathological trait associated with DR and often observed in late-stage liver diseases.[29] Consistent with this, in PCLS, periportal HNF4α$^+$ hepatocytes adjacent to the mesenchyme upregulated the biliary marker Opn after 96 h, indicating a localized metaplastic response that recapitulates the zonated pattern seen in patients[30–32] (Figure 2G and S2R). Next, we examined the stromal compartment and found that the HSC cluster could be subdivided into two distinct populations, one of which displayed a transcriptional profile consistent with activated myofibroblasts, typically associated with the DR (Figures 2B and 2C). This subset expressed smooth muscle actin (Acta2, also known as αSMA), along with the markers of proliferation, as well as induction of the YAP signaling pathway, whose involvement in myofibroblast activation has been well documented (Figures 2C, 2D, and S3A).[33] Immunofluorescence for αSMA (Figures 2H and S3B) and EdU incorporation assay confirmed the presence of proliferating myofibroblasts within PCLS, near the expanding biliary ductules (Figures 2H and 2I). Stromal cells were particularly enriched in the portal traits (Figures 2G and S3C). Finally, we examined the immune compartment and identified both lymphocytes and KC (Figure 2B). Immunofluorescence further confirmed that PCLS retained immune cells, with CD45$^+$ cells enriched in the portal areas and tissue-resident F4/80$^+$ KCs distributed within the sinusoids (Figure 2J and S3D). A more detailed analysis revealed that portal immune cells included T cells, dendritic cells, and neutrophils (Figures S3E–S3G).[34,35]

Overall, this implemented PCLS system preserves the native hepatic ECM and retains key cell populations essential for the activation and maintenance of reactive BECs, thereby ensuring that the *ex vivo* DR occurs within a native-like context that closely mimics the pathophysiology of the injured liver.

The MVA pathway is an essential regulator of DR

Metabolic pathways are increasingly recognized as key regulators of cell identity and tissue regeneration across different organs, and recent studies have shown how metabolism impacts progenitor cell proliferation and differentiation.[36] Taking advantage of the PCLS system's ability to reproduce DR onset in a physiologically relevant setting, we used this model to assess the role of key metabolic pathways in driving DR activation. To achieve this, we

(D) Violin plots illustrating the Cordenonsi signature score (YAP activation) across identified clusters.
(E) Violin plots showing the DR activation score across identified clusters.
(F) Density plot highlighting hepatocytes co-expressing *Opn* and *Hnf4a* in the UMAP space.
(G) Representative immunofluorescence staining of VIM and Opn in PCLS. Scale bars, 500 μm.
(H–J) Representative immunofluorescence staining of α-SMA (H), VIM and EdU (I), and CD45 and F4/80 (J) in PCLS. Scale bars, 50 μm.

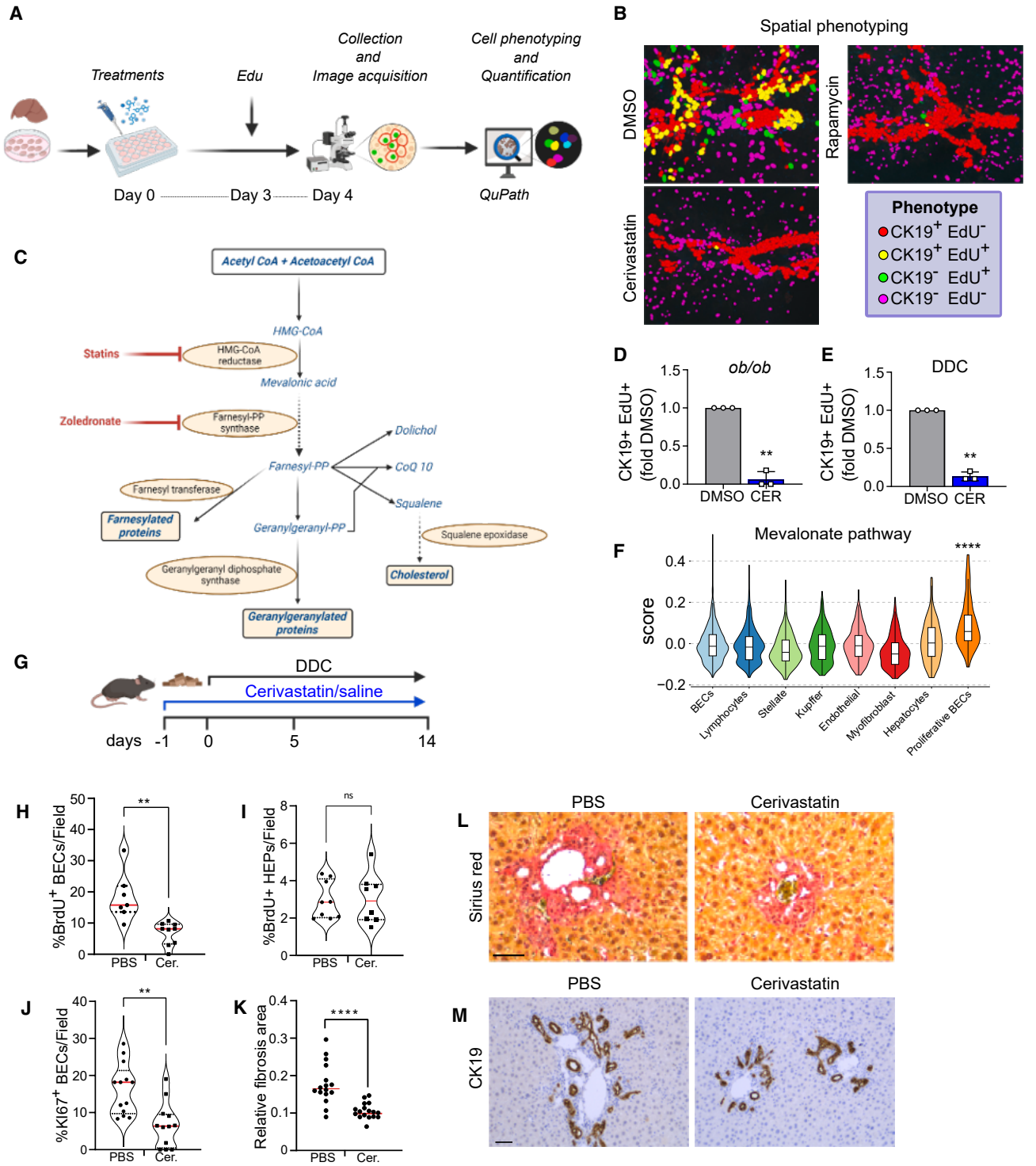

Figure 3. Functional screening and *in vivo* validation of MVA pathway blockade in BECs

(A) Schematic overview of imaging-based screening using EdU labeling and automated cell phenotyping.

(B) Spatial phenotyping of PCLS after treatment with DMSO, rapamycin, or cerivastatin.

(C) Schematic view of the MVA pathway. Metabolites are shown in blue, enzymes in black (yellow ovals), and inhibitors in red.

(D and E) Quantification of CK19-EdU double-positive biliary cells in PCLS generated from ob/ob (D) or DDC-fed (E) mice following treatment with cerivastatin ($n = 3$). A paired t test was used for statistical testing.

(legend continued on next page)

treated PCLS derived from ob/ob mice with a curated set of compounds known to target relevant liver metabolic pathways (Figure S3H). To monitor DR activation, we performed EdU incorporation assays followed by immunofluorescence and digital histology-based phenotyping, enabling automated detection and quantification of $CK19^+/EdU^+$ double-positive cells in each treatment group (Figure 3A). Confirming the reliability of our approach, we found that rapamycin, an inhibitor of the mTOR pathway and known to control reactive BECs' activation, was able to reduce the DR in PCLS[16,17] (Figures 3B and S3I). Across the various compounds tested, cerivastatin emerged among the most potent, almost completely blunting DR activation in liver slices, without affecting bile duct morphology or viability (Figures 3B and S3I). Cerivastatin belongs to a group of small-molecule drugs called statins largely used to lower cholesterol levels in patients with hypercholesterolemia through the competitive inhibition of hydroxy-3-methylglutaryl coenzyme-A reductase (HMGCR), the rate-limiting enzyme of the mevalonate (MVA) pathway[37] (Figure 3C). Through this pathway, MVA is converted into intermediates that are consequently incorporated into a variety of end-products such as cholesterol, heme A, ubiquinone, isoprenoids, bile acids, and steroid hormones.[38,39] Validation experiments demonstrated a potent inhibitory effect of statins on DR activation in PCLS from ob/ob mice as well as in DR propagation in PCLS from DDC-fed mice (Figures 3D and 3E). Supporting the involvement of this pathway in DR, we found that the expression of MVA pathway genes was higher in proliferative BECs compared to the other clusters (Figure 3F; Table S4). To confirm this data, we monitored the expression of SREBP2, a master transcription factor that regulates MVA-related genes in response to metabolic and mechanical cues,[38,40] as a proxy for MVA pathway activation. We observed that SREBP2 specifically marked reactive cholangiocytes in PCLS, showing also nuclear localization—a pattern absent in biliary cells of healthy livers—suggesting predominant activation in DR cells (Figure S4A). Next, we examined whether pharmacological inhibition of the MVA pathway affects DR induction *in vivo*. To this aim, mice were subjected to a DDC diet while simultaneously receiving cerivastatin (Figure 3G). Strikingly, we found that MVA pathway inhibition effectively prevented reactive BECs' activation while leaving hepatocyte proliferation unaffected (Figures 3H–3J and S3K). Moreover, at later time points, statin treatment led to a marked reduction of periportal fibrosis (Figures 3K–3M). Consistently, administration of the widely prescribed atorvastatin to DDC-fed mice reduced both DR and plasma alanine aminotransferase (ALT) levels (Figures S3L and S3M), reflecting improved liver function.

Together, these data validate the potential of the PCLS model as a reliable and versatile tool to identify regulatory mechanisms of DR and that the MVA pathway is required for the activation of BECs, both *ex vivo* and *in vivo*.

MVA-derived cholesterol and GGPP in BECs fuel the DR

DR can be driven by intrinsic, cell-autonomous mechanisms within BECs, as well as by indirect cues from the surrounding microenvironment, including paracrine signals released by activated stromal cells (e.g., interleukin-6 and TWEAK) or direct physical interactions between mesenchymal cells and BECs.[5,11] In line with previously published data, we found that, in addition to reactive BECs, statins also reduced the proliferation of mesenchymal cells, suggesting a broader inhibitory effect on key cell populations involved in DR[41] (Figure S3J). This evidence raised the question of whether statins inhibit DR through direct effects on reactive BECs or indirectly via stromal cell inhibition. To address this, we leveraged cholangiocyte organoids (COs), a simplified 3D culture system consisting solely of reactive BECs[42] (Figures 4A and S4B–S4E). Of note, statin treatment blunted the proliferative potential of COs in a dose-dependent manner, showing significant effects even at clinically relevant doses (Figures 4B and 4C). The impact of MVA inhibition on organoid proliferation was also confirmed by an EdU assay (Figure 4D) and using an additional, FDA-approved statin (i.e., simvastatin, Sim.) (Figure 4E). Accordingly, treatment with zoledronate (Zol.), an FDA-approved farnesyl diphosphate synthase inhibitor, an enzyme acting downstream of HMGCR in the MVA pathway, phenocopied the effect of cerivastatin on organoid growth (Figure 4E). These findings indicate that MVA pathway inhibitors suppress the DR, at least in part, through a direct effect on proliferating reactive BECs.

To rule out the possibility that inhibition of COs' proliferation induced by statins reflects a general toxic effect due to interference with an essential metabolic pathway in hepatic cells, we induced differentiation of mouse COs in hepatocyte-like cells using a previously designed differentiation medium (Figures 4F and S4F).[22,42] This condition led to a significant reduction in cell proliferation alongside the acquisition of hepatocyte-like features. In this differentiated, low-proliferative state, organoids became insensitive to statin treatment, indicating that the impact of MVA pathway inhibition is selective for actively proliferating biliary cells (Figure 4F). Interestingly, differentiation induced a marked reduction in the expression of MVA pathway genes (Figure 4G).

Next, we sought to identify the MVA-derived metabolites required for BEC proliferation (Figure 3C). Among the MVA

(F) Violin plots showing the activation score of the MVA pathway across clusters identified in Figure 2B. A *t* test was used for statistical testing (proliferative chol vs. all the other clusters).
(G) Mice were fed a DDC diet for 5 or 14 days, and cerivastatin ($n = 4$) or saline solution ($n = 4$) was intraperitoneally injected starting 24 h before administering the DDC diet.
(H) $BrdU^+$ BECs were quantified following the treatment. An unpaired *t* test was used for statistical testing.
(I) $BrDU^+$ hepatocytes were quantified following the treatment. An unpaired *t* test was used for statistical testing.
(J) Quantification of $Ki67^+$ BECs in the same livers. An unpaired *t* test was used for statistical testing.
(K) Hepatic collagen quantification in mice fed DDC for 14 days. An unpaired *t* test was used for statistical testing.
(L) Representative images of Sirius red staining in DDC-fed mouse. Scale bars, 40 μm.
(M) Representative immunohistochemical staining of CK19 in mice fed DDC for 14 days. Scale bars, 40 μm.
p value summary: ns not statistically significant, $^{**}p < 0.01$, and $^{****}p < 0.0001$.

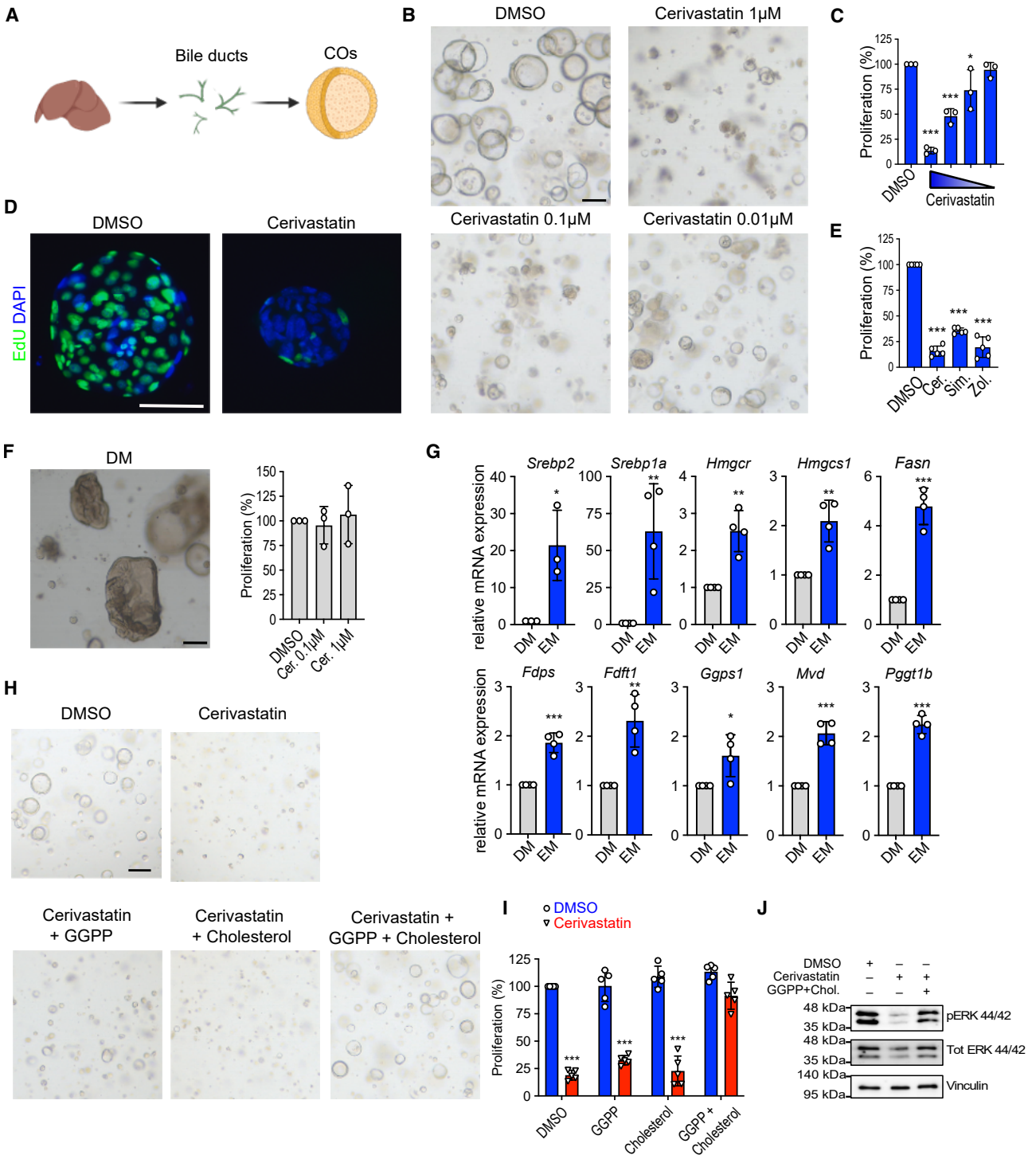

Figure 4. Cerivastatin impairs the viability and proliferation of COs through MVA pathway inhibition

(A) COs were generated from the mouse liver.

(B) Representative brightfield images of COs upon treatment with cerivastatin for 72 h. Scale bars, 100 μm.

(C) Quantification of COs' proliferation ($n = 3$). A one-way ANOVA was used for statistical testing, $p < 0.0001$. Dunnet's post hoc test was used for multiple comparisons.

(D) Representative immunofluorescence staining of EdU in COs.

(legend continued on next page)

pathway intermediates, cholesterol and geranylgeranyl pyrophosphate (GGPP) are reported to play key roles in cell fate determination and proliferation.[43,44] Cholesterol is a major component of plasma and organelle membranes, while GGPP is essential for the prenylation of many proteins involved in cell polarity, trafficking, proliferation, and survival. Thus, we investigated the contribution of both cholesterol and GGPP in mediating the DR-inhibitory effect of statins. The addition of either cholesterol or GGPP to statin-treated COs could not rescue the organoid growth (Figures 4H and 4I). However, the combined addition of both intermediates to the medium completely rescued the proliferation in organoids, demonstrating that these metabolites are concomitantly required for reactive BECs' proliferation (Figures 4H and 4I). Given that both cholesterol and GGPP are essential for DR induction, we reasoned that cholesterol likely supports cell proliferation by serving as a structural building block for plasma membrane biosynthesis, whereas GGPP could act by regulating specific proliferative signaling pathways. Among these, ERK1/2, downstream effectors of the mitogen-activated protein kinase cascade, are known regulators of cell proliferation whose activation state is indirectly modulated by intracellular GGPP levels.[16,45] Thus, we investigated whether ERK activation serves as a downstream signaling axis through which GGPP and cholesterol cooperate to sustain DR. Of note, statin treatment significantly suppressed ERK phosphorylation in COs, an effect fully reversed by supplementation with both cholesterol and GGPP (Figure 4J).

Collectively, these findings support a model in which reactive BECs, endowed with metabolic plasticity, reprogram MVA biosynthesis to sustain proliferation through cholesterol- and GGPP-dependent activation of ERK1/2, and that pharmacological inhibition of this pathway by statins is sufficient to suppress the DR, unveiling an unexpected metabolic vulnerability of reactive biliary cells.

PCLS from human livers model a DR *ex vivo* within a preserved microenvironment

We next extended our investigation to a more clinically relevant context by generating PCLS from fresh human liver samples (hPCLS), with variable degrees of disease (Table S1). These hPCLS were cultured in the same EM used for mouse PCLS, further enriched with factors previously identified as necessary for human reactive BECs' expansion (human EM)[46] (Figure 5A). EdU assay revealed that, regardless of the initial disease state, hPCLS allowed the proliferation and the expansion of $CK7^+$ biliary cells over time, with frequencies ranging from 10% to 40% across patients (Figures 5B, S5A, and S5B). These cells expanded mainly within the portal area, particularly at the interface with the parenchyma, a pattern commonly seen in human DR (Figure 5H). Sirius red staining and second harmonic generation (SHG) imaging showed that portal architecture and collagen content were preserved in hPCLS, with stable collagen fiber features (Figures S5C–S5E). To characterize the hepatic cellular landscape in hPCLS, we conducted snRNA-seq analysis of patient-derived slices, retrieving 6,008 nuclei (Figures 5C, S6A, and S6B). Integration within a recently published human snRNA-seq dataset spanning the full spectrum of MASLD progression (Figure S6C) revealed that hPCLS retain all major hepatic cell types—albeit in varying proportions (Figure S6D). Interestingly, BECs derived from hPCLS clustered more closely with those from end-stage human liver disease rather than with healthy livers, indicating the maintenance or acquisition of a reactive pathological phenotype (Figure S6E). Indeed, a detailed inspection of the BEC cluster in hPCLS revealed the presence of a significant number of proliferating BECs expressing a high level of YAP signature (Figures 5C and 5E; Table S4). Notably, BECs showed an elevated expression of DR markers, including NCAM1, TNFRSF12A, JAG1, and CXCL5 (Figures 5D and 5F; Table S4). Comparison with healthy and MASLD livers showed that PCLS-derived cholangiocytes diverged from the shared core and occupied distinct clusters enriched for either DR or proliferation markers (Figures S6F–S6H). Finally, BECs in PCLS showed a strong activation of the MVA pathway signature (Figure 5G; Table S4).

Focusing on parenchymal cells, we found the presence of biphenotypic hepatocytes expressing biliary markers, consistent with observations made in mouse PCLS (Figure S6I). snRNA-seq and immunofluorescence also confirmed the presence of abundant ACTA2-expressing myofibroblasts within hPCLS and clearly revealed physical interactions between biliary and stromal cells—interactions known to regulate DR activation[11] (Figures 5H and S6B). However, the immune compartment in hPCLS was limited and primarily composed of KCs, which is consistent with the lack of immune cell infiltration observed in the liver tissue from which the slices were originally derived (Figure 5C). As proof of principle of the potential of hPCLS to preserve an inflammatory ecosystem within the PCLS, we derived slices from a patient exhibiting pronounced hepatic immune infiltration. We then performed single-cell RNA sequencing (scRNA-seq), which enables a more comprehensive and accurate profiling of immune cell populations.[47] As expected, the analysis confirmed the presence of immune cells, which was further

(E) Quantification of COs proliferation upon treatment with either cerivastatin, simvastatin, or zoledronate ($n = 5$). A one-way ANOVA was used for statistical testing, $p < 0.0001$. Dunnet's post hoc test was used for multiple comparisons.
(F) Representative brightfield image of differentiated COs (left). Scale bars, 100 μm. Quantification of differentiated COs proliferation upon cerivastatin treatment for 72 h (right) ($n = 3$). A one-way ANOVA was used for statistical testing: p = n.s.
(G) Gene expression analysis of MVA pathway-related genes in mouse COs. Expression data are presented as mean ± SD ($n = 4$). Unpaired t test was used for statistical testing.
(H) Representative brightfield images of COs upon treatments for 72 h. Scale bars, 50 μm.
(I) Quantification of Cos' proliferation ($n = 5$). A two-way ANOVA was used for statistical testing: column factor (statin treatment) $p < 0.0001$ and row factor (rescue) $p < 0.0001$. Tukey's post hoc test was used for multiple comparisons.
(J) Representative immunoblot analysis showing ERK phosphorylation in mouse COs treated for 24 h ($n = 3$ biological replicates).
p value summary: n.s. $p > 0.05$, $^*p < 0.05$, $^{**}p < 0.01$, and $^{***}p < 0.001$.
Abbreviations: Cer., cerivastatin; Chol: cholesterol; DM, differentiation medium; EM, expansion medium; Sim., simvastatin; and Zol., zoledronate.

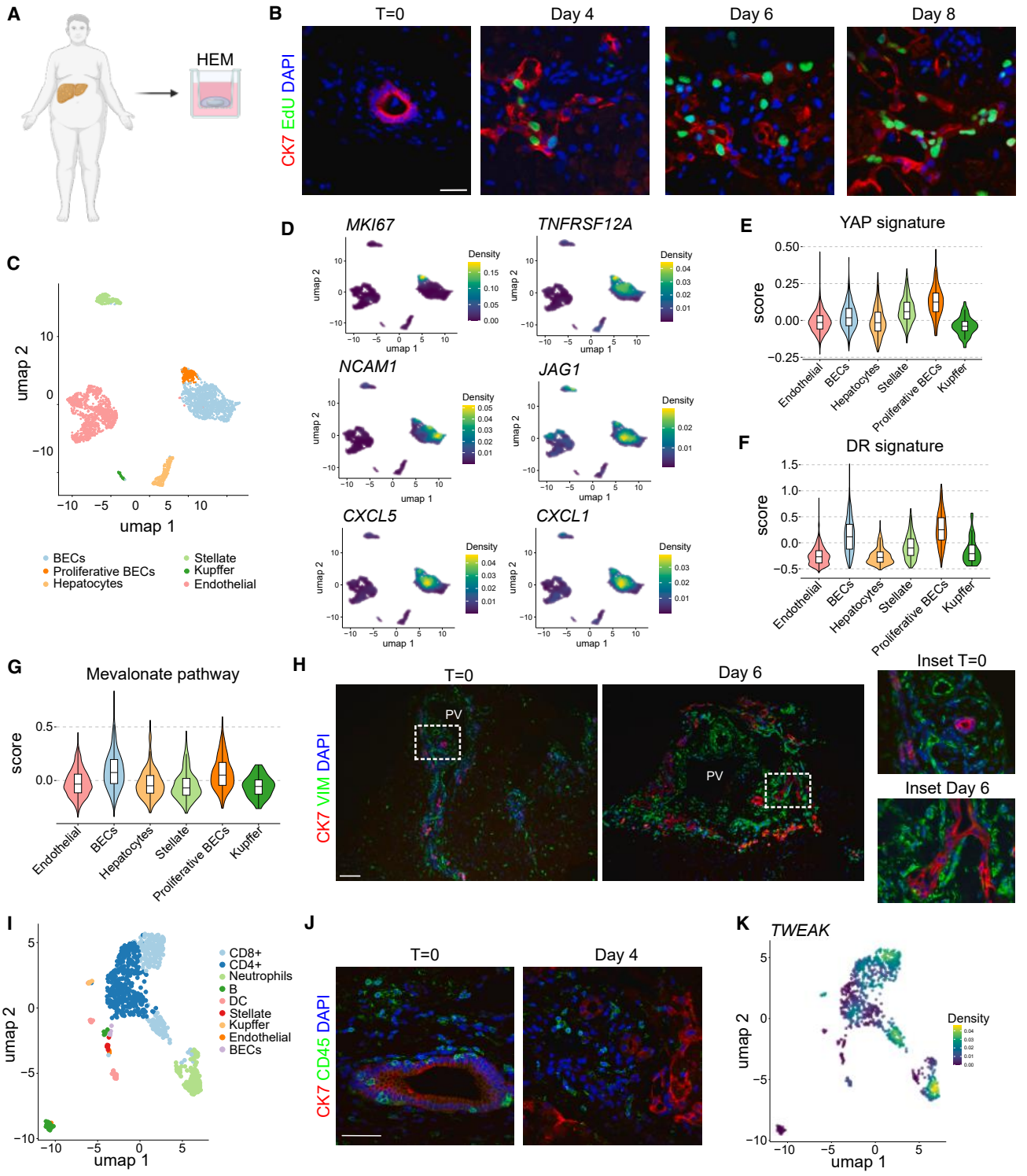

Figure 5. *Ex vivo* expansion of BECs in human PCLS and cellular composition of the DR niche

(A) Overview of PCLS establishment from human liver specimens.

(B) Representative immunofluorescence staining of CK7 and EdU in human PCLS during culture. Scale bars, 50 μm.

(C) UMAP projection showing cell annotation of single nuclei from human PCLS after quality control.

(legend continued on next page)

validated by immunofluorescence staining for the pan-leukocyte marker CD45 (Figure 5I, 5J, S6J, and S6K). $CD8^+$, $CD4^+$ T lymphocytes, and neutrophils were the most abundant immune cells within hPCLS (Figure 5I and S6K). Of note, we found that immune cells, such as $CD8^+$ lymphocytes and neutrophils, expressed elevated levels of TWEAK (Figure 5K). This is particularly relevant as TWEAK is a key paracrine regulator of DR, acting on its receptor TNFRSF12A, which is highly expressed in reactive cells (Figure 5D).[35,48]

Collectively, these results demonstrate that hPCLS effectively model a DR *ex vivo*, in a patient-specific manner, preserving a rich and diverse cellular landscape within a physiologically relevant microenvironment that reflects the original *in vivo* condition.

Human DR cells exhibit MVA pathway activation and are vulnerable to its inhibition

To evaluate the therapeutic potential of statins in mitigating the DR in human reactive BECs, we generated 16 human intrahepatic CO (hCO) lines obtained from hepatic resections of obese patients and subjected them to statin treatment (Figure 6A). Notably, we found that statin treatment successfully reduced organoid proliferation *ex vivo* in all tested organoids (Figures 6A and 6B). Mirroring the trends observed in mouse organoids, the response of hCO to statins exhibited a dose-dependent relationship, with the efficacy markedly diminishing upon the induction of quiescence (Figures S7A–S7C). Importantly, the administration of cholesterol and GGPP to statin-treated organoids efficiently rescued hCOs' proliferation, underscoring the pivotal involvement of the two metabolites in this regulatory mechanism (Figures 6A and 6B).

To explore the potential link between MVA pathway activation and the DR in patients with MASLD, we interrogated a recently published snRNA-seq dataset (Gribben et al.) comprising 47 liver biopsies from different stages of MASLD.[4] In this study, DR induction was clearly evident at the transcriptional level in BECs from end-stage diseased livers, as shown by the upregulation of established DR markers and numerous YAP targets[4] (Figure 6C). Of note, we found that MVA pathway genes were similarly induced, with a progressive upregulation in BECs toward end-stage disease (Figure 6C). Moreover, the induction of some of the MVA pathway genes preceded the overt DR, suggesting a functional role in BECs' activation.

To extend our investigation of the MVA pathway activation beyond MASLD, we explored PSC as a distinct pathological context associated with pronounced DR. PSC is a rare, immune-mediated cholangiopathy marked by progressive bile duct injury and prominent ductular expansion. Given the scarcity of available samples, our analysis was restricted to archived histological sections from a small cohort of PSC patients in which biliary proliferation was confirmed by histological assessment (Table S2). As a proxy for MVA pathway activation, we assessed the expression of SREBP2. Immunofluorescence analysis revealed a consistent nuclear accumulation of SREBP2 in DR cells, indicating active engagement of the MVA pathway in reactive BECs of PSC livers (Figure S8A). In line with this observation, we identified SREBP2 among the genes specifically expressed in the subpopulation of activated human BECs, in a published metadata analysis of mouse and human livers.[49]

Finally, we investigated whether patients with MASLD taking statins might be protected from DR activation. To this aim, we assembled a cohort of patients with MASLD and categorized them based on their use of statins at the time of histological assessment. The two groups did not differ in terms of fibrosis stage (Figure S7D), ensuring a meaningful comparison of DR extent without confounding variables. Remarkably, DR was significantly less pronounced in patients treated with statins (Figure 6D). Furthermore, consistent with our *ex vivo* results in PCLS, the number of portal myofibroblasts and pro-inflammatory macrophages was significantly lower in statin-treated patients (Figures 6D and S7E).

Together, these findings identify MVA pathway activation as a central node in DR pathogenesis and propose statins as a potential therapeutic approach to mitigate DR-driven liver pathology in chronic liver diseases.

DISCUSSION

Although DR has emerged as a promising therapeutic target, the underlying mechanisms remain complex and poorly understood. To address this knowledge gap and facilitate the identification of novel potential drug candidates, we here developed a novel *ex vivo* model of mouse and human DR, based on precision-cut liver slices, that offers significant advantages compared to previous systems. The first strength of our platform is its ability to capture multiple aspects of liver complexity. It preserves the geometric architecture of the portal microenvironment, enabling the study of BECs' activation within a native pathophysiological spatial context, providing valuable insights into the spatiotemporal dynamics of this complex biological process. Secondly, this novel culture system is multicellular, encompassing not only epithelial but also stromal and immune cells, which collectively orchestrate the initiation and propagation of the DR. Our snRNA-seq and scRNA-seq analyses in both mouse and human samples revealed that PCLS retain a rich and diverse hepatic cellular ecosystem. Importantly, snRNA-seq analysis highlighted the emergence of reactive BECs with a strong DR and YAP signature, along with evidence of hepatocyte transdifferentiation, further supporting the fidelity of the model in recapitulating

(D) Density plots displaying the expression of representative marker genes of DR for each cluster across the UMAP space in (C).
(E) Violin plots illustrating the Cordenonsi signature score (YAP activation) across identified clusters.
(F) Violin plots showing the DR activation score across identified clusters.
(G) Violin plots showing the activation score of the MVA pathway across identified clusters.
(H) Representative immunofluorescence staining of CK7 and VIM in human PCLS. Scale bars, 100 μm. PV, portal vein.
(I) UMAP projection showing cell annotation of single cells from human PCLS after quality control.
(J) Representative immunofluorescence staining of CK7 and CD45 in human PCLS. Scale bars, 50 μm.
(K) Density plots displaying the expression of TWEAK across the UMAP space in (I).

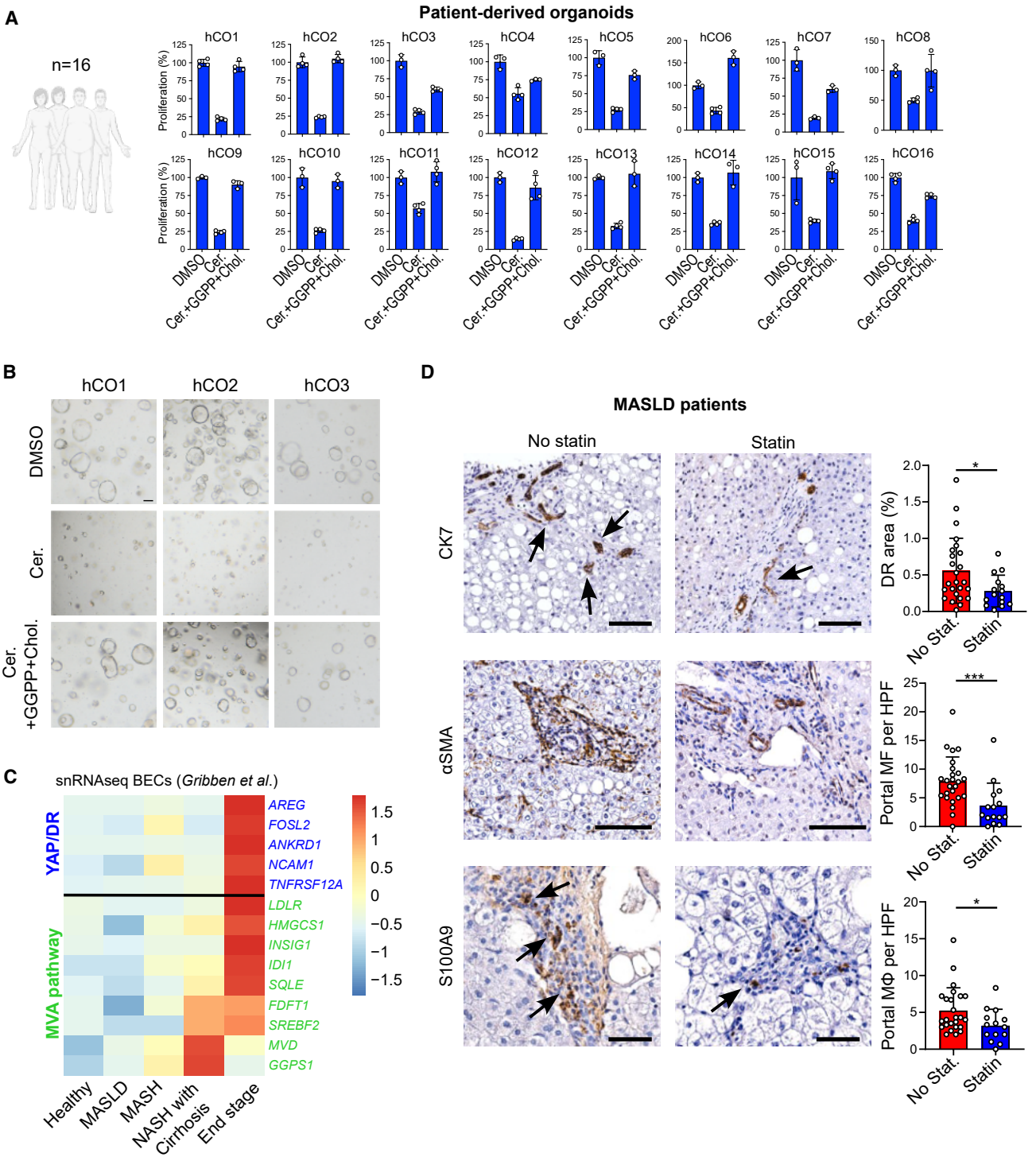

Figure 6. Human DR cells exhibit MVA pathway activation and are vulnerable to its inhibition

(A) Quantification of hCO viability upon treatment with cerivastatin alone or in combination with GGPP and cholesterol. Each chart depicts hCO generated from an individual patient. Viability data are presented as mean ± SD. (n = 3–4 technical replicates).

(B) Representative brightfield images relative to (A). Scale bars, 100 μm.

(C) Heatmap showing relative expression of DR markers, YAP target genes, and MVA pathway genes across disease stages in cholangiocytes from publicly available snRNA-seq.

(legend continued on next page)

the pathophysiological features of DR. Moreover, scRNA-seq revealed the retention of a complex immune compartment actively expressing DR-promoting signaling molecules such as TWEAK and JAG1. These data confirm that PCLS enables a high-resolution interrogation of DR across epithelial, stromal, and immune compartments, in both murine and human samples.

Due to the capacity to maintain the fibrotic properties of the peri-portal area as native, this model offers a unique advantage in investigating the DR onset in a physiologically relevant mechanical context, a feature that allowed us to identify the MVA pathway, known for its sensitivity to mechanical cues, as a crucial regulator of cholangiocyte activation. Our evidence that the inhibition of the MVA pathway prevents DR initiation in mouse and human livers provides a proof of principle of the translational relevance of this technology and suggests that statins may offer therapeutic benefits in patients with DR-associated liver diseases, including PSC and MASLD.[50] In line with this notion, the beneficial effect of statins in PSC and MASLD patients is already supported by several retrospective clinical studies. For example, a large population-based study conducted in Sweden recently found that patients taking statins had a significantly lower risk of developing PSC compared to those who did not take statins.[51,52] Similarly, a large recent multicenter study showed that statin use in patients with MASLD was associated with reduced liver-related clinical events and liver stiffness progression, as assessed by transient elastography.[53] While this population-based evidence highlights the clinical relevance of statins, our study provides mechanistic insight into how statins may exert these beneficial effects by directly targeting the metabolic dependencies of DR. Supporting this notion, our analysis of liver biopsies from patients with MASLD showed that statin use was associated with reduced DR and decreased myofibroblast activation. Although a substantial proportion of patients with MASLD are already on statin therapy due to associated metabolic risk factors, many others remain untreated despite clear clinical indications.[54] Considering the well-established safety profile of these drugs, this study reinforces the importance of statin use in this population, not only for cardiovascular protection but also for their role in suppressing DR, thereby providing a rationale for evaluating their use even in patients with MASLD and PSC without established cardiovascular disease.

The evidence that the MVA pathway is activated in DR cells is in line with current knowledge that the transition of facultative adult stem cells from quiescence to proliferation involves fundamental changes in cellular function, including metabolic adaptations, to support stemness and tissue regeneration.[16,55,56] In this context, the role of the MVA pathway as a gatekeeper of epithelial damage has been found in different biological contexts via mechanisms involving both cholesterol and GGPP biosynthesis.[39,57,58] More generally, there is a growing recognition of the role of lipid metabolism in biliary cell activation and proliferation, and our findings in DR align with this emerging understanding, further supporting the significance of lipid metabolism in cholangiopathies.

In conclusion, the organotypic model presented in this study represents a novel, important tool for investigating the molecular mechanisms of DR and unveils an unexpected role of the MVA pathway in BECs' activation, suggesting the therapeutic potential of statins in preventing DR-associated liver diseases.

Limitations of the study

This model has some limitations, including spontaneous hepatocyte necrosis that limits the study of hepatocyte physiology, the need for further optimization of stromal and immune cell maintenance, and the relative rarity of BECs within the slices, which may constrain some applications but still enables reliable assessment of DR dynamics.

RESOURCE AVAILABILITY

Lead contact

Further information and requests for resources and reagents should be directed to and will be fulfilled by the lead contact, Dr. Giovanni Sorrentino (giovanni.sorrentino@units.it).

Materials availability

All reagents generated in this study are accessible from the lead contact with a completed materials transfer agreement.

Data and code availability

- The sequencing data and raw expression matrix are available on the Gene Expression Omnibus, series entry GEO: GSE295943.
- This paper does not report original code.
- Any additional information required to reanalyze the data reported in this paper is available from the lead contact upon request.

ACKNOWLEDGMENTS

The authors thank all the members of ADM and CCS labs at ICGEB for insightful discussions and Barbara Boziglav, Chiara Agostinis, and Paola Zarattini for technical support. The figures and the graphical abstract in this work were created with BioRender (https://BioRender.com). G.S. is funded by grants from AIRC (Start-Up 2020 – ID. 24322 project – PI S.G.), Telethon (GGP20031), and the Italian Ministry of University and Research and European Union under NextGenerationEU ("Progetti di rilevante interesse nazionale" [PRIN]: PRIN prot. no. 2022PWKZXE and PNRR M4C2 INV 1.1, PRIN 2022 prot. no. P2022A9J9L). G.D.S. and G.S. are supported by the NRRP NextGenerationEU project CN00000041-National Center for Gene Therapy and Drugs based on RNA Technology and Worldwide Cancer Research (WWCR) grant 24-0361. G.D.S. is supported by the Fondazione AIRC IG grants 22174 and 30570 and the Fondazione AIRC Special Program Molecular Clinical Oncology "5 per mille" grant 22759. E.G. was funded by the Italian Ministry of University and Research ("Progetti di rilevante interesse nazionale": PRIN-2022HT2MAT) and by Sapienza University of Rome (Bandi di Ricerca di Ateneo). D.O. was funded by the Italian Ministry of University and Research ("PRIN PNRR P2022H7JYZ). F.C. is funded by grants from WWCR (grant no. 23-0321) and the European Union under NextGenerationEU, PRIN 2022 (prot. no. 2022PWKZXE). E.F. was supported by the Veronica Graziani AIRC fellowship for Italy. N.R. and P.G. were supported by an intramural research

(D) Immunohistochemistry and respective positive area quantification for CK 7 (upper), αSMA (middle), and S100A9 (lower) in liver biopsies obtained from patients with MASLD under statin therapy regimen or not (n = 15 and 25, respectively). Arrows indicate positive cells. Scale bars, 100 μm in upper and middle rows; and 50 μm in the lower row.

Data are presented as means ± SD. An unpaired t test was used for statistical analysis. p value summary: $^{*}p < 0.05$, $^{**}p < 0.01$, and $^{***}p < 0.001$. Abbreviations: HPF, high-powered field; MF, myofibroblast; and MΦ, macrophages.

grant from the Italian Liver Foundation. R. Bertolio was supported by an AIRC fellowship for Italy.

AUTHOR CONTRIBUTIONS

Conceptualization, G.S. and B.A.; methodology, B.A., S.V., D.S., C.G., E.F., G.B., P.P., D.O., and R. Bertolio; investigation, B.A., S.V., D.S., C.G., E.F., G.B., P.P., D.O., and R. Bertolio; writing – original draft, B.A., S.V., D.S., and G.S.; writing – review & editing, B.A., S.V., D.S., C.G., E.F., G.B., P.P., D.O., R. Bulla, L.C., C.T., E.G., G.D.S., G.C., F.C., and G.S.; funding acquisition, G.S.; resources, A.S., M.B., N.C., F.B., M.D.B., P.G., N.R., M.M., P.T., M.P., F.Z., N.d.M., S.P., and D.B.; and supervision, L.C., C.T., E.G., G.D.S., G.C., F.C., and G.S.

DECLARATION OF INTERESTS

G.S. and B.A. are inventors on a patent application filed by UNITS covering aspects of methods described in this study.

DECLARATION OF GENERATIVE AI AND AI-ASSISTED TECHNOLOGIES IN THE WRITING PROCESS

During the preparation of this work, the authors used ChatGPT to improve clarity and streamline the text to meet the journal's space constraints. After using this tool, the authors reviewed and edited the content as needed and take full responsibility for the content of the publication.

STAR★METHODS

Detailed methods are provided in the online version of this paper and include the following:

- KEY RESOURCES TABLE
- EXPERIMENTAL MODEL AND STUDY PARTICIPANT DETAILS
  - Human liver samples and ethics statements
  - Experimental animal models
  - Preparation of precision-cut liver slices
  - Mouse and human cholangiocyte organoids generation
- METHOD DETAILS
  - PCLS treatment with compounds
  - PCLS viability
  - Composition of cholangiocyte organoids culture media
  - Organoid treatments and viability assay
  - Transaminase quantification
  - Histological analysis
  - Immunohistochemistry
  - Immunohistochemistry quantification
  - Immunofluorescence
  - Image acquisition
  - Proliferation assay
  - Quantification of proliferating BEC in PCLS
  - Second harmonic generation microscopy
  - Quantitative real-time qRT-PCR for mRNA quantification
  - Western blotting
  - Single nuclei isolation
  - Single cell RNA sequencing library preparation
  - Data processing and QC
  - Normalization and annotation of cells
  - Pathway analysis and signature scoring
  - Publicly available dataset analysis
- QUANTIFICATION AND STATISTICAL ANALYSIS

SUPPLEMENTAL INFORMATION

Supplemental information can be found online at https://doi.org/10.1016/j.celrep.2025.116681.

Received: May 13, 2025
Revised: September 16, 2025
Accepted: November 17, 2025
Published: December 12, 2025

REFERENCES

1. Raven, A., Lu, W.Y., Man, T.Y., Ferreira-Gonzalez, S., O'Duibhir, E., Dwyer, B.J., Thomson, J.P., Meehan, R.R., Bogorad, R., Koteliansky, V., et al. (2017). Cholangiocytes act as facultative liver stem cells during impaired hepatocyte regeneration. Nature *547*, 350–354. https://doi.org/10.1038/nature23015.
2. Sorrentino, G. (2025). Microenvironmental control of the ductular reaction: balancing repair and disease progression. Cell Death Dis. *16*, 246. https://doi.org/10.1038/s41419-025-07590-4.
3. Gupta, V., Sehrawat, T.S., Pinzani, M., and Strazzabosco, M. (2025). Portal Fibrosis and the Ductular Reaction: Pathophysiological Role in the Progression of Liver Disease and Translational Opportunities. Gastroenterology *168*, 675–690. https://doi.org/10.1053/j.gastro.2024.07.044.
4. Gribben, C., Galanakis, V., Calderwood, A., Williams, E.C., Chazarra-Gil, R., Larraz, M., Frau, C., Puengel, T., Guillot, A., Rouhani, F.J., et al. (2024). Acquisition of epithelial plasticity in human chronic liver disease. Nature *630*, 166–173. https://doi.org/10.1038/s41586-024-07465-2.
5. Sato, K., Marzioni, M., Meng, F., Francis, H., Glaser, S., and Alpini, G. (2019). Ductular Reaction in Liver Diseases: Pathological Mechanisms and Translational Significances. Hepatology *69*, 420–430. https://doi.org/10.1002/hep.30150.
6. Cai, X., Tacke, F., Guillot, A., and Liu, H. (2023). Cholangiokines: undervalued modulators in the hepatic microenvironment. Front. Immunol. *14*, 1192840. https://doi.org/10.3389/fimmu.2023.1192840.
7. Azad, A.I., Krishnan, A., Troop, L., Li, Y., Katsumi, T., Pavelko, K., Kostallari, E., Guicciardi, M.E., and Gores, G.J. (2020). Targeted Apoptosis of Ductular Reactive Cells Reduces Hepatic Fibrosis in a Mouse Model of Cholestasis. Hepatology *72*, 1013–1028. https://doi.org/10.1002/hep.31211.
8. Clerbaux, L.A., Manco, R., Van Hul, N., Bouzin, C., Sciarra, A., Sempoux, C., Theise, N.D., and Leclercq, I.A. (2019). Invasive Ductular Reaction Operates Hepatobiliary Junctions upon Hepatocellular Injury in Rodents and Humans. Am. J. Pathol. *189*, 1569–1581. https://doi.org/10.1016/j.ajpath.2019.04.011.
9. Aguilar-Bravo, B., Rodrigo-Torres, D., Ariño, S., Coll, M., Pose, E., Blaya, D., Graupera, I., Perea, L., Vallverdú, J., Rubio-Tomás, T., et al. (2019). Ductular Reaction Cells Display an Inflammatory Profile and Recruit Neutrophils in Alcoholic Hepatitis. Hepatology *69*, 2180–2195. https://doi.org/10.1002/hep.30472.
10. Cordero-Espinoza, L., and Huch, M. (2018). The balancing act of the liver: tissue regeneration versus fibrosis. J. Clin. Investig. *128*, 85–96. https://doi.org/10.1172/JCI93562.
11. Cordero-Espinoza, L., Dowbaj, A.M., Kohler, T.N., Strauss, B., Sarlidou, O., Belenguer, G., Pacini, C., Martins, N.P., Dobie, R., Wilson-Kanamori, J.R., et al. (2021). Dynamic cell contacts between periportal mesenchyme and ductal epithelium act as a rheostat for liver cell proliferation. Cell Stem Cell *28*, 1907–1921.e8. https://doi.org/10.1016/j.stem.2021.07.002.
12. Cadamuro, M., Lasagni, A., Sarcognato, S., Guido, M., Fabris, R., Strazzabosco, M., Strain, A.J., Simioni, P., Villa, E., and Fabris, L. (2022). The Neglected Role of Bile Duct Epithelial Cells in NASH. Semin. Liver Dis. *42*, 34–47. https://doi.org/10.1055/s-0041-1739455.
13. Sancho-Bru, P., Altamirano, J., Rodrigo-Torres, D., Coll, M., Millán, C., José Lozano, J., Miquel, R., Arroyo, V., Caballería, J., Ginès, P., and Bataller, R. (2012). Liver progenitor cell markers correlate with liver damage and predict short-term mortality in patients with alcoholic hepatitis. Hepatology *55*, 1931–1941. https://doi.org/10.1002/hep.25614.
14. Krishnan, A., Katsumi, T., Guicciardi, M.E., Azad, A.I., Ozturk, N.B., Trussoni, C.E., and Gores, G.J. (2020). Tumor Necrosis Factor-Related

Apoptosis-Inducing Ligand Receptor Deficiency Promotes the Ductular Reaction, Macrophage Accumulation, and Hepatic Fibrosis in the Abcb4(-/-) Mouse. Am. J. Pathol. *190*, 1284–1297. https://doi.org/10.1016/j.ajpath.2020.02.013.

15. Omenetti, A., and Diehl, A.M. (2011). Hedgehog signaling in cholangiocytes. Curr. Opin. Gastroenterol. *27*, 268–275. https://doi.org/10.1097/MOG.0b013e32834550b4.
16. Aloia, L., McKie, M.A., Vernaz, G., Cordero-Espinoza, L., Aleksieva, N., van den Ameele, J., Antonica, F., Font-Cunill, B., Raven, A., Aiese Cigliano, R., et al. (2019). Epigenetic remodelling licences adult cholangiocytes for organoid formation and liver regeneration. Nat. Cell Biol. *21*, 1321–1333. https://doi.org/10.1038/s41556-019-0402-6.
17. Planas-Paz, L., Sun, T., Pikiolek, M., Cochran, N.R., Bergling, S., Orsini, V., Yang, Z., Sigoillot, F., Jetzer, J., Syed, M., et al. (2019). YAP, but Not RSPO-LGR4/5, Signaling in Biliary Epithelial Cells Promotes a Ductular Reaction in Response to Liver Injury. Cell Stem Cell *25*, 39–53.e10. https://doi.org/10.1016/j.stem.2019.04.005.
18. Lorenzini, S., Bird, T.G., Boulter, L., Bellamy, C., Samuel, K., Aucott, R., Clayton, E., Andreone, P., Bernardi, M., Golding, M., et al. (2010). Characterisation of a stereotypical cellular and extracellular adult liver progenitor cell niche in rodents and diseased human liver. Gut *59*, 645–654. https://doi.org/10.1136/gut.2009.182345.
19. Saxton, S.H., and Stevens, K.R. (2023). 2D and 3D liver models. J. Hepatol. *78*, 873–875. https://doi.org/10.1016/j.jhep.2022.06.022.
20. Olinga, P., and Schuppan, D. (2013). Precision-cut liver slices: a tool to model the liver ex vivo. J. Hepatol. *58*, 1252–1253. https://doi.org/10.1016/j.jhep.2013.01.009.
21. de Graaf, I.A.M., Olinga, P., de Jager, M.H., Merema, M.T., de Kanter, R., van de Kerkhof, E.G., and Groothuis, G.M.M. (2010). Preparation and incubation of precision-cut liver and intestinal slices for application in drug metabolism and toxicity studies. Nat. Protoc. *5*, 1540–1551. https://doi.org/10.1038/nprot.2010.111.
22. Huch, M., Dorrell, C., Boj, S.F., van Es, J.H., Li, V.S.W., van de Wetering, M., Sato, T., Hamer, K., Sasaki, N., Finegold, M.J., et al. (2013). In vitro expansion of single Lgr5+ liver stem cells induced by Wnt-driven regeneration. Nature *494*, 247–250. https://doi.org/10.1038/nature11826.
23. Voabil, P., de Bruijn, M., Roelofsen, L.M., Hendriks, S.H., Brokamp, S., van den Braber, M., Broeks, A., Sanders, J., Herzig, P., Zippelius, A., et al. (2021). An ex vivo tumor fragment platform to dissect response to PD-1 blockade in cancer. Nat. Med. *27*, 1250–1261. https://doi.org/10.1038/s41591-021-01398-3.
24. Wang, X., Lopategi, A., Ge, X., Lu, Y., Kitamura, N., Urtasun, R., Leung, T.M., Fiel, M.I., and Nieto, N. (2014). Osteopontin induces ductular reaction contributing to liver fibrosis. Gut *63*, 1805–1818. https://doi.org/10.1136/gutjnl-2013-306373.
25. Coombes, J.D., Swiderska-Syn, M., Dollé, L., Reid, D., Eksteen, B., Claridge, L., Briones-Orta, M.A., Shetty, S., Oo, Y.H., Riva, A., et al. (2015). Osteopontin neutralisation abrogates the liver progenitor cell response and fibrogenesis in mice. Gut *64*, 1120–1131. https://doi.org/10.1136/gutjnl-2013-306484.
26. Roskams, T., Yang, S.Q., Koteish, A., Durnez, A., DeVos, R., Huang, X., Achten, R., Verslype, C., and Diehl, A.M. (2003). Oxidative stress and oval cell accumulation in mice and humans with alcoholic and nonalcoholic fatty liver disease. Am. J. Pathol. *163*, 1301–1311. https://doi.org/10.1016/S0002-9440(10)63489-X.
27. Yildiz, E., El Alam, G., Perino, A., Jalil, A., Denechaud, P.D., Huber, K., Fajas, L., Auwerx, J., Sorrentino, G., and Schoonjans, K. (2023). Hepatic lipid overload triggers biliary epithelial cell activation via E2Fs. eLife *12*, e81926. https://doi.org/10.7554/eLife.81926.
28. Dewyse, L., De Smet, V., Verhulst, S., Eysackers, N., Kunda, R., Messaoudi, N., Reynaert, H., and van Grunsven, L.A. (2022). Improved Precision-Cut Liver Slice Cultures for Testing Drug-Induced Liver Fibrosis. Front. Med. *9*, 862185. https://doi.org/10.3389/fmed.2022.862185.
29. Sirica, A.E. (1995). Ductular hepatocytes. Histol. Histopathol. *10*, 433–456.
30. Yanger, K., Zong, Y., Maggs, L.R., Shapira, S.N., Maddipati, R., Aiello, N.M., Thung, S.N., Wells, R.G., Greenbaum, L.E., and Stanger, B.Z. (2013). Robust cellular reprogramming occurs spontaneously during liver regeneration. Genes Dev. *27*, 719–724. https://doi.org/10.1101/gad.207803.112.
31. Nakanuma, Y., and Ohta, G. (1986). Immunohistochemical study on bile ductular proliferation in various hepatobiliary diseases. Liver *6*, 205–211. https://doi.org/10.1111/j.1600-0676.1986.tb01067.x.
32. Van Eyken, P., Sciot, R., and Desmet, V.J. (1988). A cytokeratin immunohistochemical study of alcoholic liver disease: evidence that hepatocytes can express 'bile duct-type' cytokeratins. Histopathology *13*, 605–617. https://doi.org/10.1111/j.1365-2559.1988.tb02092.x.
33. Mannaerts, I., Leite, S.B., Verhulst, S., Claerhout, S., Eysackers, N., Thoen, L.F.R., Hoorens, A., Reynaert, H., Halder, G., and van Grunsven, L.A. (2015). The Hippo pathway effector YAP controls mouse hepatic stellate cell activation. J. Hepatol. *63*, 679–688. https://doi.org/10.1016/j.jhep.2015.04.011.
34. Van Hul, N., Lanthier, N., Español Suñer, R., Abarca Quinones, J., van Rooijen, N., and Leclercq, I. (2011). Kupffer cells influence parenchymal invasion and phenotypic orientation, but not the proliferation, of liver progenitor cells in a murine model of liver injury. Am. J. Pathol. *179*, 1839–1850. https://doi.org/10.1016/j.ajpath.2011.06.042.
35. Bird, T.G., Lu, W.Y., Boulter, L., Gordon-Keylock, S., Ridgway, R.A., Williams, M.J., Taube, J., Thomas, J.A., Wojtacha, D., Gambardella, A., et al. (2013). Bone marrow injection stimulates hepatic ductular reactions in the absence of injury via macrophage-mediated TWEAK signaling. Proc. Natl. Acad. Sci. USA *110*, 6542–6547. https://doi.org/10.1073/pnas.1302168110.
36. Solhi, R., Lotfinia, M., Gramignoli, R., Najimi, M., and Vosough, M. (2021). Metabolic hallmarks of liver regeneration. Trends Endocrinol. Metab. *32*, 731–745. https://doi.org/10.1016/j.tem.2021.06.002.
37. Demierre, M.F., Higgins, P.D.R., Gruber, S.B., Hawk, E., and Lippman, S.M. (2005). Statins and cancer prevention. Nat. Rev. Cancer *5*, 930–942. https://doi.org/10.1038/nrc1751.
38. Goldstein, J.L., and Brown, M.S. (1990). Regulation of the mevalonate pathway. Nature *343*, 425–430. https://doi.org/10.1038/343425a0.
39. Wang, B., Rong, X., Palladino, E.N.D., Wang, J., Fogelman, A.M., Martín, M.G., Alrefai, W.A., Ford, D.A., and Tontonoz, P. (2018). Phospholipid Remodeling and Cholesterol Availability Regulate Intestinal Stemness and Tumorigenesis. Cell Stem Cell *22*, 206–220.e4. https://doi.org/10.1016/j.stem.2017.12.017.
40. Bertolio, R., Napoletano, F., Mano, M., Maurer-Stroh, S., Fantuz, M., Zannini, A., Bicciato, S., Sorrentino, G., and Del Sal, G. (2019). Sterol regulatory element binding protein 1 couples mechanical cues and lipid metabolism. Nat. Commun. *10*, 1326. https://doi.org/10.1038/s41467-019-09152-7.
41. Santos, D.M., Pantano, L., Pronzati, G., Grasberger, P., Probst, C.K., Black, K.E., Spinney, J.J., Hariri, L.P., Nichols, R., Lin, Y., et al. (2020). Screening for YAP Inhibitors Identifies Statins as Modulators of Fibrosis. Am. J. Respir. Cell Mol. Biol. *62*, 479–492. https://doi.org/10.1165/rcmb.2019-0296OC.
42. Broutier, L., Andersson-Rolf, A., Hindley, C.J., Boj, S.F., Clevers, H., Koo, B.K., and Huch, M. (2016). Culture and establishment of self-renewing human and mouse adult liver and pancreas 3D organoids and their genetic manipulation. Nat. Protoc. *11*, 1724–1743. https://doi.org/10.1038/nprot.2016.097.
43. Mullen, P.J., Yu, R., Longo, J., Archer, M.C., and Penn, L.Z. (2016). The interplay between cell signalling and the mevalonate pathway in cancer. Nat. Rev. Cancer *16*, 718–731. https://doi.org/10.1038/nrc.2016.76.
44. Sorrentino, G., Ruggeri, N., Specchia, V., Cordenonsi, M., Mano, M., Dupont, S., Manfrin, A., Ingallina, E., Sommaggio, R., Piazza, S., et al. (2014).

Metabolic control of YAP and TAZ by the mevalonate pathway. Nat. Cell Biol. *16*, 357–366. https://doi.org/10.1038/ncb2936.

45. Yanae, M., Tsubaki, M., Satou, T., Itoh, T., Imano, M., Yamazoe, Y., and Nishida, S. (2011). Statin-induced apoptosis via the suppression of ERK1/2 and Akt activation by inhibition of the geranylgeranyl-pyrophosphate biosynthesis in glioblastoma. J. Exp. Clin. Cancer Res. *30*, 74. https://doi.org/10.1186/1756-9966-30-74.
46. Huch, M., Gehart, H., van Boxtel, R., Hamer, K., Blokzijl, F., Verstegen, M.M.A., Ellis, E., van Wenum, M., Fuchs, S.A., de Ligt, J., et al. (2015). Long-term culture of genome-stable bipotent stem cells from adult human liver. Cell *160*, 299–312. https://doi.org/10.1016/j.cell.2014.11.050.
47. Wen, F., Tang, X., Xu, L., and Qu, H. (2022). Comparison of single-nucleus and single-cell transcriptomes in hepatocellular carcinoma tissue. Mol. Med. Rep. *26*, 339. https://doi.org/10.3892/mmr.2022.12855.
48. Jakubowski, A., Ambrose, C., Parr, M., Lincecum, J.M., Wang, M.Z., Zheng, T.S., Browning, B., Michaelson, J.S., Baetscher, M., Wang, B., et al. (2005). TWEAK induces liver progenitor cell proliferation. J. Clin. Investig. *115*, 2330–2340. https://doi.org/10.1172/JCI23486.
49. Verhulst, S., Roskams, T., Sancho-Bru, P., and van Grunsven, L.A. (2019). Meta-Analysis of Human and Mouse Biliary Epithelial Cell Gene Profiles. Cells *8*, 1117. https://doi.org/10.3390/cells8101117.
50. Liao, J.K., and Laufs, U. (2005). Pleiotropic effects of statins. Annu. Rev. Pharmacol. Toxicol. *45*, 89–118. https://doi.org/10.1146/annurev.pharmtox.45.120403.095748.
51. Stokkeland, K., Hoijer, J., Bottai, M., Soderberg-Lofdal, K., and Bergquist, A. (2019). Statin Use Is Associated With Improved Outcomes of Patients With Primary Sclerosing Cholangitis. Clin. Gastroenterol. Hepatol. *17*, 1860–1866.e1861. https://doi.org/10.1016/j.cgh.2018.11.002.
52. Annika Bergquist, H.-U.M., Nilsson, E., Nyhlin, N., Werner, M., Amanda, Klein, M.B., Kechagias, S., and Rorsman, F. (2022). Long Term Effect of Simvastatin in Primary Sclerosing Cholangitits: A Placebo-Controlled, Double-Blind, Multicenter Phase III Study (Piscatin). Br. J. Gastroenterol. *4*, 235–241. https://doi.org/10.31488/bjg.1000128.
53. Zhou, X.D., Kim, S.U., Yip, T.C.F., Petta, S., Nakajima, A., Tsochatzis, E., Boursier, J., Bugianesi, E., Hagström, H., Chan, W.K., et al. (2024). Long-term liver-related outcomes and liver stiffness progression of statin usage in steatotic liver disease. Gut *73*, 1883–1892. https://doi.org/10.1136/gutjnl-2024-333074.
54. Zhou, X.-D., Muthiah, M.D., and Zheng, M.-H. (2025). Statins in MASLD: Challenges and future directions. JHEP Rep. *7*, 101372. https://doi.org/10.1016/j.jhepr.2025.101372.
55. Yuan, W., and Song, C. (2020). The Emerging Role of Rab5 in Membrane Receptor Trafficking and Signaling Pathways. Biochem. Res. Int. *2020*, 4186308. https://doi.org/10.1155/2020/4186308.
56. Shapira, S.N., and Christofk, H.R. (2020). Metabolic Regulation of Tissue Stem Cells. Trends Cell Biol. *30*, 566–576. https://doi.org/10.1016/j.tcb.2020.04.004.
57. Li, X., Wu, J.B., Li, Q., Shigemura, K., Chung, L.W.K., and Huang, W.C. (2016). SREBP-2 promotes stem cell-like properties and metastasis by transcriptional activation of c-Myc in prostate cancer. Oncotarget *7*, 12869–12884. https://doi.org/10.18632/oncotarget.7331.
58. Pan, Q., Zhong, S., Wang, H., Wang, X., Li, N., Li, Y., Zhang, G., Yuan, H., Lian, Y., Chen, Q., et al. (2021). The ZMYND8-regulated mevalonate pathway endows YAP-high intestinal cancer with metabolic vulnerability. Mol. Cell *81*, 2736–2751.e8. https://doi.org/10.1016/j.molcel.2021.04.009.
59. Lee, S., Ren, L., Li, W., Paranjpe, A., Zhou, P., Potter, A., Huppert, S.S., and Shin, S. (2025). Rbpj deletion in hepatic progenitor cells attenuates endothelial responses and fibrosis in DDC-fed mice. Hepatol. Commun. *9*, e0745. https://doi.org/10.1097/HC9.0000000000000745.
60. Carlessi, R., Denisenko, E., Boslem, E., Köhn-Gaone, J., Main, N., Abu Bakar, N.D.B., Shirolkar, G.D., Jones, M., Beasley, A.B., Poppe, D., et al. (2023). Single-nucleus RNA sequencing of pre-malignant liver reveals disease-associated hepatocyte state with HCC prognostic potential. Cell Genom. *3*, 100301. https://doi.org/10.1016/j.xgen.2023.100301.
61. Bankhead, P., Loughrey, M.B., Fernández, J.A., Dombrowski, Y., McArt, D.G., Dunne, P.D., McQuaid, S., Gray, R.T., Murray, L.J., Coleman, H.G., et al. (2017). QuPath: Open source software for digital pathology image analysis. Sci. Rep. *7*, 16878. https://doi.org/10.1038/s41598-017-17204-5.
62. Bredfeldt, J.S., Liu, Y., Pehlke, C.A., Conklin, M.W., Szulczewski, J.M., Inman, D.R., Keely, P.J., Nowak, R.D., Mackie, T.R., and Eliceiri, K.W. (2014). Computational segmentation of collagen fibers from second-harmonic generation images of breast cancer. J. Biomed. Opt. *19*, 16007. https://doi.org/10.1117/1.JBO.19.1.016007.
63. Hao, Y., Stuart, T., Kowalski, M.H., Choudhary, S., Hoffman, P., Hartman, A., Srivastava, A., Molla, G., Madad, S., Fernandez-Granda, C., and Satija, R. (2024). Dictionary learning for integrative, multimodal and scalable single-cell analysis. Nat. Biotechnol. *42*, 293–304. https://doi.org/10.1038/s41587-023-01767-y.
64. Rinella, M.E., Lazarus, J.V., Ratziu, V., Francque, S.M., Sanyal, A.J., Kanwal, F., Romero, D., Abdelmalek, M.F., Anstee, Q.M., Arab, J.P., et al. (2023). A multisociety Delphi consensus statement on new fatty liver disease nomenclature. J. Hepatol. *79*, 1542–1556. https://doi.org/10.1016/j.jhep.2023.06.003.
65. European Association for the Study of the Liver EASL; European Association for the Study of Diabetes EASD; European Association for the Study of Obesity EASO (2024). EASL-EASD-EASO Clinical Practice Guidelines on the management of metabolic dysfunction-associated steatotic liver disease (MASLD). J. Hepatol. *81*, 492–542. https://doi.org/10.1016/j.jhep.2024.04.031.
66. European Association for the Study of the Liver EASL; European Association for the Study of Diabetes EASD; European Association for the Study of Obesity EASO (2016). EASL-EASD-EASO Clinical Practice Guidelines for the management of non-alcoholic fatty liver disease. J. Hepatol. *64*, 1388–1402. https://doi.org/10.1016/j.jhep.2015.11.004.
67. Bedossa, P.; FLIP Pathology Consortium (2014). Utility and appropriateness of the fatty liver inhibition of progression (FLIP) algorithm and steatosis, activity, and fibrosis (SAF) score in the evaluation of biopsies of nonalcoholic fatty liver disease. Hepatology *60*, 565–575. https://doi.org/10.1002/hep.27173.
68. Overi, D., Carpino, G., Cristoferi, L., Onori, P., Kennedy, L., Francis, H., Zucchini, N., Rigamonti, C., Viganò, M., Floreani, A., et al. (2022). Role of ductular reaction and ductular-canalicular junctions in identifying severe primary biliary cholangitis. JHEP Rep. *4*, 100556. https://doi.org/10.1016/j.jhepr.2022.100556.
69. Carpino, G., Del Ben, M., Pastori, D., Carnevale, R., Baratta, F., Overi, D., Francis, H., Cardinale, V., Onori, P., Safarikia, S., et al. (2020). Increased Liver Localization of Lipopolysaccharides in Human and Experimental NAFLD. Hepatology *72*, 470–485. https://doi.org/10.1002/hep.31056.
70. Uwe Schmidt, M.W., Coleman, B., and Myers, G. (2018). Cell Detection with Star-Convex Polygons (Springer International Publishing), pp. 265–273.

STAR★METHODS

KEY RESOURCES TABLE

REAGENT or RESOURCE	SOURCE	IDENTIFIER
Antibodies		
CD11c	Cell Signaling	97585; RRID: AB_2800282
CD45	Abcam	ab10558; RRID: AB_442810
CD45	R&D system	AF114; RRID: AB_44214
CK19	Abcam	ab133496; RRID: AB_11155282
CK19	Santa Cruz biotechnology	sc-376126; RRID: AB_10988034
CK7	Santa Cruz biotechnology	sc-23876; RRID: AB_2265604
CK7	Dako	M7018; RRID: AB_2134589
F4/80	Santa Cruz biotechnology	sc-52664; RRID: AB_629466
HNF4α	Abcam	ab199431; RRID: AB_3271581
Ki67	Abcam	ab16667; RRID: AB_302459
Ly6G	Cell Signaling	87048; RRID: AB_2909808
BrdU	Abcam	ab6326; RRID: AB_2313786
Opn	Bio-techne	AF808; RRID: AB_2194992
Phospho-p44/42 MAPK (Erk1/2) (Thr202/Tyr204)	Cell Signaling	4370; RRID: AB_2315112
p44/42 MAPK (Erk1/2)	Cell Signaling	9102; RRID: AB_330744
S100A9	Abcam	ab92507; RRID: AB_10562628
SREBP2	Abcam	ab30682; RRID: AB_779079
Vimentin	Abcam	ab92547; RRID: AB_10562134
Vinculin	Santa Cruz biotechnology	sc-73614; RRID: AB_1131294
α-SMA	Abcam	ab5694; RRID: AB_2223021
α-SMA	Dako	M0851; RRID:AB_2223500
Chemicals, peptides, and recombinant proteins		
Cultrex Basal Membrane Extract (BME) Type 2	Biotechne,	3533-010-02
DMEM/F-12	Sigma-Aldrich	SCM162
B27 supplement	Thermo Fisher Scientific	12587010
N2 supplement	Thermo Fisher Scientific	17502048
N-acetylcysteine (NAC)	Sigma-Aldrich	A9165
recombinant human Rspondin-1 (Rspo1)	Pepro Tech	120–38
Nicotinamide	Sigma-Aldrich	N0636
recombinant human [Leu15]-gastrin I	Sigma-Aldrich	G9145
recombinant mouse EGF	Pepro Tech	315–09
recombinant human HGF	Pepro Tech	100-39H
recombinant human FGF10	GenScript	z03314
Forskolin	BioGems	6652995
A83-01	BioGems	9094360
recombinant human Noggin	Pepro Tech	120-10C
recombinant human Wnt3a	HumanKine	HZ1296
Y-27632	MCE	HY-10583
Cerivastatin	Sigma-Aldrich	SML0005
simvastatin	Sigma-Aldrich	S6196
zoledronate	Vinci-Biochem	BVN-B3110-1

(*Continued on next page*)

Continued

REAGENT or RESOURCE	SOURCE	IDENTIFIER
C75	Cayman	10005270
MF-438	Cayman	33349
IBMX	Cayman	13347
compound C	Sigma-Aldrich	171260
2-deoxy-D-Glucose	Cayman	14325
UK5099	Cayman	16980
etomoxir	Cayman	11969
compound 968	Cayman	17199
rapamicyn	Cayman	13346
dexamethasone	Sigma-Aldrich	D4902
DAPT	BioGems	2088055
BMP7	Pepro Tech	120-03P
recombinant human FGF19	Pepro Tech	100–32
Geranylgeranyl Pyrophosphate	Cayman	63330
cholesterol	Sigma-Aldrich	S5442
Prolong® gold	Thermo Fisher Scientific	P36934
TrypLE Express	Gibco	12604013
BrdU	Sigma-Aldrich	B9285
PowerTrack™ SYBR™ green master mix	Applied biosystem	A46109
Critical commercial assays		
ALT assay kit	Abnova	KA4189
CellTiter-Glo luminescent cell viability kit	Promega	G6081
Click-iT EdU Cell Proliferation Kit	Thermo Fisher Scientific	C10337
ReadyProbes™ Tissue Autofluorescence Quenching kit	Thermo Fisher Scientific	R37630
NucleSpin Tissue kit	Macherey-Nagel	740952
high-capacity RNA-to-cDNA kit	Applied biosystem	4387406
Deposited data		
Human scRNA-seq, mouse and human snRNA-seq data	This study	GEO: GSE295943
Human snRNA-seq	Gribben et al.[4]	GEO: GSE202379
Mouse (DDC diet) snRNA-seq	Lee et al.[59]	GEO: GSE296940
Mouse (chow diet) snRNA-seq	Carlessi et al.[60]	GEO: GSE200366
Experimental models: Organisms/strains		
Mouse: C57BL/6 wild type	The Jackson Laboratory	https://www.jax.org/strain/000664
Mouse: B6.Cg-Lepob/J (ob/ob)	The Jackson Laboratory	https://www.jax.org/strain/000632
Oligonucleotides		
qPCR primers used in this study	Table S7	N/A
Software and algorithms		
QuPath (version 0.5.1)	Bankhead et al.[61]	https://qupath.github.io/
ImageJ (version 1.54f)	NIH	https://imagej.net/ij/
BioRender	–	https://www.biorender.com/
Graphpad prism 10	Graphpad	https://www.graphpad.com/
ct-FIRE v.2.0b	Bredfeldt et al.[62]	https://loci.wisc.edu/software/ctFIRE
R	R foundation	Version 4.4.1
RStudio	R foundation	Version 2025.5.1.513
Seurat	Hao et al.[63]	Version 5.0.2

EXPERIMENTAL MODEL AND STUDY PARTICIPANT DETAILS

Human liver samples and ethics statements

Liver samples used for organotypic cultures were non-tumoral tissues from patients undergoing tumor resection or surgical resections (wedge biopsy) performed in a cohort of morbidly obese subjects enrolled in a bariatric surgery program by the Department of Surgery at the University Hospital of Trieste (Italy). Sensitive data were protected through anonymization. The generation of organotypic cultures was approved by the ethical committee of the region Friuli Venezia Giulia (''comitato etico unico regionale'') (protocol n. 0033969, 26/08/2024). Informed written consent was obtained from all subjects involved in the study. Patients' characteristics are summarized in Table S1.

Paraffin-embedded primary sclerosing cholangitis biopsies were provided by the children's hospital ''Burlo Garofolo-IRCCS'' (Trieste, Italy). Parents signed informed consent at the first visit, agreeing that ''clinical data may be used for clinical research purposes, epidemiology, the study of pathologies and training, to improve knowledge, care, and prevention''. The data were collected according to the Authorization to Process Personal Data for Scientific Research Purposes (Authorization no. 9/2014) approved by the ethical committee of the children's hospital ''Burlo Garofolo-IRCCS'' and was in accordance with the Declaration of Helsinki. Patients' characteristics are summarized in Table S2.

For MASLD cohort in Figure 6D, we included consecutive outpatients presenting with cardio-metabolic risk factors, referring to the Day Service of Internal Medicine at the Umberto I - University Hospital in Rome and screened by ultrasound for the presence of fatty liver; patients with ultrasound evidence of fatty liver and persistent elevation of transaminases >6 months underwent liver biopsies (n = 86). Diagnosis of MASLD was based on established criteria.[64,65] Liver biopsies were collected, and histo-pathological analysis was performed. Samples were selected to include only patients with definite MASH. The diagnosis of definite steatohepatitis (i.e., MASH) was based on FLIP algorithm at biopsy.[66,67] Only patients with MASH and available information on statin therapy regimen were included (N = 40). Based on statin therapy regimen, patients were divided into two groups: no statin [N = 25; M/F = 14/11; Age: 53 (IQR: 46–58)] and statin [N = 15; M/F = 7/8; Age: 53 (IQR: 51–59)]. Patient groups did not differ in term of age and gender. The study protocol conformed to the ethical guidelines of the Declaration of Helsinki and was approved by the local ethical board of Sapienza University of Rome (ref. 2277 prot. 873/11). Informed written consent was obtained from all subjects involved in the study.

Experimental animal models

C57BL/6 wild type and B6.Cg-Lepob/J (ob/ob) mice were housed under standard conditions with a 12-h day/night cycle in a pathogen-free environment with access to food and water *ad libitum* at the animal facility of the University of Trieste (Italy). 4-month-old C57BL/6 wild type mice were fed a 0.1% 3,5-diethoxycarbonyl-1,4-dihydrocollidine (DDC) diet (Mucedola srl, Italy) for three weeks to induce ductular reaction. Liver tissue was collected from DDC-fed mice,5-month-old homozygous B6.Cg-Lepob/J, and C57BL/6 wild type mice immediately after scarification with carbon dioxide and processed as described below.

For *in vivo* studies, C57BL/6 wild-type mice were fed a 0.1% 3,5-diethoxycarbonyl-1,4-dihydrocollidine (DDC) diet (Mucedola srl, Italy) to induce ductular reaction. In the short experiment, eight animals received the DDC diet for four days and were treated intraperitoneally with Cerivastatin (20 mg/kg; Sigma, SML0005) (n = 4) or vehicle (saline) (n = 4) once daily, starting 24 h before diet administration. In the long experiment, eight mice were maintained on the DDC diet for two weeks and treated intraperitoneally with Cerivastatin (20 mg/kg) (n = 4) or vehicle (n = 4) every two days, starting 24 h before diet administration. In both experimental settings, 5-bromo-2′-deoxyuridine (BrdU; 100 mg/kg; Sigma, B9285) was administered intraperitoneally 2 h before sacrifice. In a third experiment, ten mice were fed the DDC diet for seven days and received Atorvastatin (20 mg/kg; Sigma, SML3030) (n = 5) or vehicle (PEG400) (n = 5) daily via oral gavage.

All animal procedures were performed in adherence with the National Institute of Health guidelines and European Community directives on the use of laboratory animals and were approved by the ethical committee of the University of Trieste, the ethical committee of the University of Trento, and responsible administration of the Ministry of Health under the authorization n° 73/2022-PR (Trieste) and n° 200/2024-PR (Trento).

Preparation of precision-cut liver slices

Precision-cut liver slices (PCLS) were prepared from human and mouse liver tissue as previously described with some modifications.[21] Immediately after resection, the hepatic specimens were transferred into sterile ice-cold basal William's E (BWE) medium (2 mM L-glutamine, 25 mM glucose, 10 mM HEPES, 1% Penicillin/Streptomycin) and kept on ice until further processing. Tissue cores were prepared using a 5 mm diameter biopsy punch and embedded in 4% low-gelling agarose (Sigma, A4018). 260-μm-thick tissue slices were prepared using a Krumdieck Tissue Slicer (TSE system, USA) and transferred into cold BWE immediately after slicing. After the cutting procedure, PCLS were incubated at 37°C, 5% CO2 for 2 h of recovery. During the recovery time, PCLS were placed in agitation for 5 min at RT every 25 min. PCLS were then embedded between two layers of Cultrex Basal Membrane Extract (BME), Type 2 (Biotechne, 3533-010-02) diluted 1:3 in BWE. The bottom layer was deposited onto an 8-μm pore polycarbonate transwell insert (Corning, 3422) and let to solidify at 37°C. After 30 min, one PCLS was gently placed on the top of the matrix and covered with a layer of diluted BME. PCLS were cultured in BWE or in expansion medium (EM) at 37°C and 5% CO2. Media were changed daily.

The mouse EM is the BWE medium supplemented with 1:50 B27 supplement (Thermo Fisher, 12587010), 1 mM N-acetylcysteine (Sigma, A9165), 1 μg/mL Rspo1 (Pepro Tech, 120-38), 10 mM nicotinamide (Sigma, N0636), 10 nM recombinant human [Leu15]-gastrin I (Sigma, G9145), 50 ng/mL recombinant mouse EGF (Pepro Tech, 315-09), 100 ng/mL recombinant human FGF10 (GenScript, z03314) and 50 ng/mL recombinant human HGF (Pepro Tech, 100-39H).

The human EM is the BWE medium supplemented with 1:50 B27 supplement, 1:100 N2 supplement (Thermo Fisher, 17502048), 1 mM N-acetylcysteine, 1 μg/mL Rspo1 (Pepro Tech, 120-38), 10 mM nicotinamide, 10 nM recombinant human [Leu15]-gastrin I, 50 ng/mL recombinant human EGF (Pepro Tech, AF-100-15), 100 ng/mL recombinant human FGF10, 25 ng/mL recombinant human HGF, 10 μM Forskolin (BioGems, 6652995), 5 μM A83-01 (BioGems, 9094360), 25 ng/mL recombinant human Noggin (Pepro Tech, 120-10C), 50 ng/mL recombinant human Wnt3a (HumanKine, H 1296).

Mouse and human cholangiocyte organoids generation

Hepatic cholangiocyte organoids were isolated from either C57BL/6J mouse livers or human biopsies following established protocols41 with minor modifications. Briefly, bile ducts were extracted from mouse livers by incubating the minced liver pieces in mouse liver digestion buffer (0.125 mg/mL collagenase and 0.125 mg/mL dispase II in DMEM) for 45–120 min at 37°C under continuous agitation. Ductal structures were separated from the undigested tissue by centrifugation and resuspended 25 μL BME droplets in 24-well plates. For human organoids, human biopsies were placed in William's E medium and transported to the laboratory on ice. Liver samples were then minced into small-cell clusters and digested in human digestion buffer (2.5 mg/mL collagenase D and 0.1 mg/mL DNaseI in Hanks' balanced salt solution) at 37°C for 75–120 min under continuous agitation. Cell clusters were separated from the undigested tissue by centrifugation and resuspended 25 μL BME droplets in 24-well plates. Following BME solidification, 500 μL of either mouse or human liver isolation media was added. Once the bile ducts started budding, isolation medium was substituted with liver expansion medium. The medium was changed every 2–3 days. Fully grown organoids were enzymatically dissociated as single cells using TrypLE Express (Gibco, 12604013) before being resuspended in BME and cultured in respective expansion medium supplemented with 10 μM Y-27632 (MCE, HY-10583) for the initial 3 days.

METHOD DETAILS

PCLS treatment with compounds

PCLS were generated from one mouse as described and immediately exposed to compounds diluted at their final concentration in EM. The medium was replaced every 24 h and samples were collected after 96 h of treatment for further analysis. To evaluate cell proliferation, PCLS were pulsed with EdU (Thermo Fisher, C10337) 24 h before collection. Two slices were treated with each compound, and dimethyl sulfoxide (DMSO)-treated PCLS were used as solvent control.

The final compound concentrations were: 1 μM cerivastatin (Sigma, SML0005), 50 μM C75 (Cayman, 10005270), 10 μM MF-438 (Cayman, 33349), 25 μM IBMX (Cayman, 13347), 0.5 μM compound C (Sigma, 171260), 5 mM 2-deoxy-D-Glucose (Cayman14325), 10 μM UK5099 (Cayman, 16980), 5 μM etomoxir (Cayman, 11969), 5 μM compound 968 (Cayman, 17199), 10 μM BLT-1, and 100 nM rapamicyn (Cayman, 13346). Final concentrations of compounds were selected based on literature evidence.

PCLS viability

PCLS were snap frozen in 100 μL of buffer containing 500 mM Tris-HCl pH 7.8, 1 mM EDTA in distilled water and stored at −80°C until processed. For quantification, an equal volume of 500 mM Tris-HCl pH 7.8, 1 mM EDTA, 1% Triton X-100 was added to each sample. Subsequently, samples were homogenized by sonication and centrifuged at 12.000 rpm at 4°C for 5 min. ATP was determined using the CellTiter-Glo Luminescent Cell Viability Assay (Promega, G6081) according to the manufacturer's protocol, and luminescence was read with an Enspire Multimode Plate Reader (PerkinElmer).

Composition of cholangiocyte organoids culture media

The basal medium was composed of advanced DMEM/F-12 (Sigma, SCM162) supplemented with 1% penicillin/streptomycin, 1% glutamine and 10 mM HEPES.

The mouse liver expansion medium was composed of the basal medium supplemented with 1:50 B27 supplement, 1 mM N-acetylcysteine, 1 μg/mL Rspo1(Pepro Tech, 120-38), 10 mM nicotinamide, 10 nM recombinant human [Leu15]-gastrin I, 50 ng/mL recombinant mouse EGF, 100 ng/mL recombinant human FGF10 and 50 ng/mL recombinant human HGF.

The human liver expansion medium was composed of the basal medium supplemented with 1:50 B27 supplement, 1:100 N2 supplement (Thermo Fisher, 17502048), 1 mM N-acetylcysteine, 1 μg/mL Rspo1(Pepro Tech, 120-38), 10 mM nicotinamide, 10 nM recombinant human [Leu15]-gastrin I, 50 ng/mL recombinant human EGF, 100 ng/mL recombinant human FGF10, 25 ng/mL recombinant human HGF, 10 μM Forskolin and 5 μM A83-01.

The mouse liver isolation medium was composed of the mouse liver expansion medium supplemented with 100 ng/mL recombinant human Noggin and 10 μM μM Y-27632.

The human liver isolation medium was composed of the human liver expansion medium supplemented with 100 ng/mL recombinant human Noggin, 50 ng/mL recombinant humanWnt3a (HumanKine, HZ1296), and 10 μM Y-27632.

For differentiation, organoids were dissociated into single cells and seeded in BME. After 7 days of culture in organoid expansion medium, the medium was changed to differentiation medium (DM) for 12 days. Medium was changed every 2 days and supplemented with 3 μM dexamethasone (Sigma, D4902) during the last 3 days. Following differentiation, hepatocytes-like organoids were subjected to respective drug treatments. Mouse DM consists of organoid expansion medium, which no longer contains Rspo1, HGF, and NAM and instead contains 50 nM A83-01 and 10 nM DAPT (BioGems, 2088055). Human DM consists of organoid expansion medium, which no longer contains Rspo1, HGF and nicotinamide and instead contains 10 nM DAPT, 25 ng/mL BMP7 (Pepro Tech, 120-03P) and 100 ng/mL human FGF19 (Pepro Tech,100-32).

Organoid treatments and viability assay

Organoids were dissociated as single cells and resuspended in BME at a concentration of 10^6 cells/ml. $5*10^3$ cells per well were embedded in 5 μL BME drops in a 96 white multi-well plates (PerkinElmer, 6005181). Followed by overnight incubation, organoids were subjected to treatments. To perform inhibitory experiments, organoids were treated with 1 μM cerivastatin (Sigma, SML0005), 1 μM simvastatin (Sigma, S6196), 100 μM zoledronate (Vinci-Biochem, BVN-B3110-1). For dose-response experiments, organoids were treated with increasing concentrations of cerivastatin (1, 0.1, 0.01, 0.001 μM for mouse organoids and 10, 1, 0.1, 0.01 μM for human organoids). For rescue experiments, organoids were treated with 1 μM cerivastatin alone or in combination with 20 μM Geranylgeranyl Pyrophosphate (Cayman, 63330) and/or 5 μg/mL cholesterol (Sigma, S5442). Cell viability was assessed after treatments (72 h for mice and 144 h for human organoids) by measuring ATP levels with the CellTiter-Glo luminescent cell viability kit (Promega, G6081) following the manufacturer's instructions. Data are reported as the percentage of viability compared to the DMSO-treated sample.

Transaminase quantification

Plasma alanine aminotransferase (ALT) levels were measured using a commercial ALT activity assay kit (Abnova, KA4189) according to the manufacturer's instructions.

Histological analysis

PCLS were incubated in cold PBS for 10 min at 4°C to remove BME and fixed in 10% formalin for 24 h at RT. Following incubation with an increasing series of ethanol and xylene, PCLS were embedded in paraffin. Similarly, organoids were fixed in 4% PFA for 1 h at RT, washed in PBS, and embedded in 4% agarose before proceeding with dehydration and paraffin embedding. 5-μm-thick PCLS or organoid sections were processed for hematoxylin-eosin (H&E) and Sirius red staining.

For the quantification of Sirius red$^+$ areas, stained tissue samples were scanned with an Axioscan 7 (Zeiss, Germany). Positive area was calculated using QuPath software (version 0.5.1) and represented as a percentage of the total hepatic tissue area. The graphed data shows the mean ± SD from independent experiments. Two PCLS have been used for each condition (technical replicates).

Immunohistochemistry

Immunohistochemical staining was performed on 5-μm-thick PCLS sections. After dewaxing and rehydration, slides underwent antigen retrieval in heated 10 mM sodium citrate tribasic, 0.05% Tween 20 solution (pH 6.0) for 30 min. Endogenous peroxidase activity was blocked with 3% hydrogen peroxide solution for 10 min, and unspecific bounds with 1% BSA, 0.01% Triton X-100 in PBS for 1 h at RT. Samples were incubated with primary antibodies overnight in a humidified chamber at 4°C. The following day, slides were washed with PBS and incubated with HRP-conjugated secondary antibody (Bethyl Laboratories, USA) diluted 1:200 for 2 h. After two washes with PBS, samples were incubated with a DAB peroxidase substrate kit (Vector Laboratories, SK-4100) and counterstain with Mayer's hematoxylin (Sigma, MHS1).

Immunohistochemistry on human liver biopsies was performed as previously described.[68] Sections were incubated overnight at 4°C with primary antibodies against CK7, S100A9, and α-Smooth Muscle Actin. For all immunoreactions, positive and negative controls (the primary antibody was replaced with pre-immune serum) were also included. Sections were examined in a coded fashion by Leica Microsystems DM 4500 B Light, equipped with a Jenoptik Prog Res C10 Plus Videocam (Jena, Germany). Slides were further scanned by a digital scanner (Aperio Scanscope CS System, Aperio Digital Pathology, Leica Biosystems, Milan, Italy) and processed by ImageScope. The area occupied by ductular reaction was evaluated by cytokeratin 7 immunoreactivity, quantified by an image analysis algorithm, and was expressed as the percentage of the parenchymal area occupied by reactive ductules; cholangiocytes lining the interlobular bile ducts were excluded from the counts.[69] The number of S100A9+ and α Smooth Muscle Actin cells was calculated as the number of cells per High-Powered Field (HPF).

Representative images shown are from experiments independently repeated at least 3 times with consistent results.

Immunohistochemistry quantification

For the quantification of CK19$^+$ PCLS areas, stained tissue samples were scanned with an Axioscan 7 (Zeiss, Germany). CK19$^+$ area was calculated using QuPath software (version 0.5.1) and represented as a percentage of the total hepatic tissue area. The graphed data shows the mean ± SD from independent experiments. Two PCLS have been used for each condition (technical replicates).

Immunofluorescence

The immunostaining was performed on 5-μm-thick PCLS sections obtained from paraffined blocks. De-paraffinization and antigen retrieval were carried out as described in the previous paragraph. After blocking the unspecific bounds with 1% BSA, 0.01% Triton X-100 in PBS for 1 h at RT, tissues were incubated with primary antibodies overnight in a humidified chamber at 4°C. The following day, slides were washed with PBS and incubated with specific secondary antibodies conjugated with Alexa Fluor 488 or 594 (Jackson Immuno Research) at 1:200 dilution in blocking solution for 2 h at RT. Nuclei were stained with 1 μg/mL 4′,6-Diamidino-2-phenylindole dihydrochloride (DAPI) and the Prolong gold antifade mounting (Life Technology, P36934) was used to seal the coverslip.

Organoids were collected from BME and fixed in 4% PFA. After washing in PBS, fixed organoids were spotted on a glass slide and subjected to permeabilization with 0.5% Triton X-100 in PBS for 45 min. After blocking with 1% BSA and 0.01% Triton X-100 in PBS for 3 h at RT, slides were incubated with primary antibodies overnight in a humidified chamber at 4°C. Following multiple washes, the slides were subjected to incubation with specific secondary antibodies conjugated with Alexa Fluor 488 or Alexa Fluor 594 at 1:500 dilution in blocking solution for 3 h at RT. For actin staining, organoids were incubated with Phalloidin-iFluor 488 conjugate (Cayman, CAY-20549-300) for 30 min prior to nuclei staining. Nuclei were stained with 1 μg/mL DAPI and the Prolong gold antifade mounting was used to seal the coverslip.

Representative images shown are from experiments independently repeated at least 3 times with consistent results.

Image acquisition

Immunofluorescence images were acquired with an Eclipse Tie microscope (Nikon, The Netherlands) or with a confocal microscope (Zeiss, LSM 880 Airyscan). Images were processed using ImageJ software (version 1.54f).

Proliferation assay

The proliferation assay was performed using Click-iT EdU Cell Proliferation Kit (Life Technology, C10337) in accordance with the manufacturer's instructions. PCLS or organoids were incubated with 10 μM Edu dissolved in medium for 16–24 h before sample collection. Subsequently, PCLS were fixed in 10% formalin and embedded in paraffin while organoids were fixed in 4% PFA and processed for immunofluorescence as previously described. Following secondary antibodies incubation, click-iT reaction cocktail was added to the samples for 30 min at RT. Nuclei were counter-stained with 1 μg/mL DAPI and the Prolong gold antifade mounting was used to seal the coverslip.

PCLS treated with compounds were processed immediately after collection for whole mount immunofluorescence. Following treatments, PCLS were collected from BME, washed with PBS, and fixed with formalin overnight. After two washes in PBS, PCLS were impermeabilized with 0.5% Triton X-100 for 20 min and blocked with 5% BSA in PBS for 1 h at RT. Antibodies incubation and EdU staining were performed as previously described in the method section. To reduce tissue autofluorescence, PCLS were incubated for 15 min with the ReadyProbes Tissue Autofluorescence Quenching kit (Life Technology, R37630) and washed in PBS three times. Nuclei were stained with 1 μg/mL 4′,6-Diamidino-2-phenylindole dihydrochloride (DAPI), and Mowiol (81381, Merck) was used to seal the coverslip.

Quantification of proliferating BEC in PCLS

Immunofluorescence slides from FFPE-PCLS prepared for the proliferation assay were scanned using a Nikon Eclipse Ti microscope (Nikon, The Netherlands). For PCLS treated with compounds, five images for each treatment were acquired using a widefield fluorescence microscope (Zeiss Axio Observer) equipped with Apotome optics and an Axioscan 807 mono camera with a 10× magnification air objective.

Quantification of EdU^+CK19^+ cells was performed using an artificial intelligence approach using QuPath software (version 0.5.1). Specifically, we adapted the StarDist[70] extension, an open-source scripts from AKOYA Bioscience, on scanned images. Computational analysis workflow for spatial phenotyping required a training step that includes cell segmentation based on nuclear DAPI staining which identifies individual cells across the tissue, and the phenotyping of the segmented cells based on their combinatorial staining intensities. Nuclear segmentation was first performed using the deep learning method StarDist applied to the DAPI image of the tissues. After cell segmentation, the average staining intensity for each marker/channel (EdU and CK19) was calculated for every individual cell in the training section from the corresponding expression compartment (nucleus or cytoplasm), and the classifiers were assigned accordingly. Once established, classifiers were applied sequentially to the full PCLS scan to determine the total number of $CK19^+$ and EdU^+CK19^+ cells. Data are reported as mean ± SD from independent experiments. Two PCLS have been used for each condition (technical replicates).

Second harmonic generation microscopy

Second Harmonic Generation microscopy was performed at the Interdepartmental Center for Advanced Microscopy (CIMA) at the University of Trieste. To visualize collagen bundles, a water dipping lens (25×, NA 1.1) was used to deliver the excitation signal and to collect the emission signal. The collagen signal was collected using 880 nm excitation carried out with a Chameleon Ultra II femtosecond titan:sapphire laser (Coherent, Dieburg, Germany) (80 MHz, 730–1050 nm) and the images were acquired with non-descanned detector present in the $A1R^+$ MP Nikon laser tunable multiphoton confocal microscope. The forward SHG signal of the collagen fibers was detected with a 405/10 nm bandpass filter and all images were captured at 2048 × 2048 full field resolution.

Total Collagen fibers were analyzed from SHG images using the ct-FIRE software package (http://loci.wisc.edu/software/ctFIRE, v.2.0b). Three different portal regions from one patient were analyzed.

Quantitative real-time qRT-PCR for mRNA quantification

RNA was extracted from organoids or liver tissue using the NucleSpin Tissue kit (Macherey-Nagel, 740952) following the manufacturer's instructions. Reverse transcription of total RNA was performed with the high-capacity RNA-to-cDNA kit (Applied biosystem, 4387406) following manufacturer's instructions. The expression of selected genes was analyzed using the iCycler iQ real-time PCR detection system (Bio-Rad, USA) and the PowerTrack SYBR green master mix (Applied biosystem, A46109). Expression values were calculated using the ΔΔCt method with the CFX Maestro 2.2 Manager software (Bio-Rad, USA). Primers for qRT-PCR are listed in Table S2.

Western blotting

Total proteins were isolated from organoids using lysis buffer (50 mM Tris-HCl (pH 8), 150 mM NaCl, 1 mM EDTA, 0.5% Nonidet P-40, 0.05% sodium deoxycholate, and protease and phosphatase inhibitors) followed by sonication and centrifugation at 4°C for 10 min at 12,000g at 4°C. Proteins were quantified using Bradford reagent following the manufacturer's instruction. 5 μg of total proteins were separated by SDS–PAGE gel and transferred onto a nitrocellulose membrane (Millipore). Following 1 h of blocking in 5% BSA in TBST, primary antibodies incubation was performed overnight in blocking solution. After secondary HRP-conjugated antibodies (Bethyl Laboratories, USA) incubation for 1 h, target proteins were detected using the ECL kit (Thermo Fisher Scientific, 32132) and visualized in a ChemiDoc MP Imaging System (Bio-Rad, USA). HRP-conjugated Vinculin antibody was used as a loading control.

Single nuclei isolation

The single nuclei suspension from liver tissue was obtained using GEXSCOPE Single Nucleus RNA Library Kit V2 (Singleron Biotechnologies). Briefly, on ice the tissue was immersed in 1mL of cold nucleus separation solution and cut into small pieces. Further homogenization was achieved by performing 10 strokes with a loose pestle (pestle A) and a tight pestle (Pestle B) (KIMBLE KONTES Dounce Tissue Grinder, cat. nr. 885300-0002). The sample was then incubated on ice for 15 min where the state of nuclei extraction was monitored every 5 min under a light microscope. Following extraction, the nuclei suspension was filtered using a 30-μm sterile strainer (Miltenyi, cat. nr.130-098-458). The nuclei suspension was centrifuged at 200xg for 2 min at 4°C, and the supernatant was centrifuged at 500xg for 5 min at 4°C. The resulting pellet containing nuclei was resuspended in 0.25 mL of cold nuclei suspension buffer. The quality of the nuclei was assessed by Trypan Blue staining (0.4% w/v, Gibco) under a light microscope. The nuclei were counted using acridine/propidium iodide with a Luna FX7 automated cell counter (Logos Biosystems, Villeneuve d'Ascq, France).

Single cell RNA sequencing library preparation

A total of 45 000 nuclei were loaded onto a microfluidic chip (Singleron GEXSCOPE Single Nucleus RNA Library Kit V2) for a minimal capture of 10 000 nuclei. Briefly, barcoded beads containing a unique Cell Barcode were loaded into the chip, and nuclei were lysed. After nuclei lysis, polyadenylated RNA was captured onto the Barcode Beads by the poly (dT) sequence. Barcode Beads with captured mRNA molecules were collected and subjected to reverse transcription reaction. The cDNA was then amplified and QC. For scRNA-seq, six human PCLS cultured for 144 h were collected and dissociated for 3 min with TriplE. The digestion was stopped, and the cells were washed three times with PBS. A suspension of 3.5×10^5 cells/mL was prepared in PBS, and the cells underwent library preparation. The scRNA-seq libraries were constructed using the GEXSCOPE Single Cell RNA Library Kit (Singleron Biotechnology) following the manufacturer's protocol for a minimal capture of 10.000 cells. Illumina-compatible NGS libraries generated were sequenced on an Illumina NovaSeq 6000 instrument using a paired-end 150bp approach. The reads were demultiplexed on Illumina's BaseCloud, and fastq files were used to initiate data analysis.

Data processing and QC

All the original samples generated for this paper were mapped and expression levels summarized using Celescope pipeline () version 2.3.0. Human samples were mapped against the GRCh38.v1.8.0 version of the Homo sapiens genome, while mouse sample was mapped against the Mus musculus GRCm39.v1.8.0 reference genome, employing default parameters in all cases. A total of 6,095 mouse and 6,008 human nuclei were identified, along with 1,586 human cells. Seurat (v5.2.1) objects were created using genes expressed in more than three cells and cells with more than 200 features expressed. For mouse snRNA-seq, nuclei with fewer than 700 features or more than 20% of counts mapping to mitochondrial genes were excluded. For human snRNA-seq, nuclei with fewer than 1,000 features, fewer than 3,000 counts, or more than 20% of counts mapping to mitochondrial genes were excluded. In human scRNA-seq, cells with fewer than 750 features, fewer than 1,200 counts, or more than 20% of counts mapping to mitochondrial genes were excluded.

Normalization and annotation of cells

Data were normalized using Seurat SCTransform() function. Principal Component Analysis (PCA) was performed using the top 2,000 highly variable genes, and the top 20 principal components (PCs) were selected based on an elbow plot of explained variance. Clustering was performed using Seurat's FindNeighbors() and FindClusters() functions, with parameters selected according to the dataset. The clustering results were visualized using UMAP dimensionality reduction.

Differential expression analysis was performed using Seurat's FindAllMarkers() function, with genes exhibiting adjusted *p*-values <0.05 considered significant. Marker genes for each cluster were identified and analyzed to uncover cluster-specific signatures. Detailed marker lists per cluster can be found in Tables S3, S5, and S6.

Pathway analysis and signature scoring

Gene expression was analyzed for key biological pathways and signatures, including the Cordenonsi Yap1-activated proliferation signature, the mevalonate pathway, and ductular reaction markers. Gene sets for the Cordenonsi and mevalonate pathways were retrieved from MSigDB, while the ductular reaction signature was custom curated based on literature for both mouse and human. Pathway activity was quantified by calculating module scores using Seurat's AddModuleScore() function. These scores were calculated for the mevalonate, Cordenonsi, and ductular reaction gene sets, with 100 random control genes used for background correction. Pathway scores were visualized using VlnPlot. Detailed gene lists per signature can be found in Tables S4.

Publicly available dataset analysis

The human snRNA-seq dataset from Gribben et al. (GSE202379) and our human PCLS snRNA-seq dataset were merged into a single Seurat object. Similarly, the mouse snRNA-seq datasets (DDC: GSE296940, healthy: GSE200366) were combined with the mouse PCLS snRNA-seq dataset. The merged datasets were normalized using the SCTransform() function, and dimensionality reduction was first performed with principal component analysis (PCA; 50 principal components). To mitigate potential batch effects across datasets, we applied the RunHarmony() function. Finally, UMAP dimensionality reduction was used for visualization of the harmonized data.

For analysis of gene expression patterns across disease stages in the cholangiocyte subset of GSE202379 dataset, a set of genes associated with the mevalonate pathway and ductular reaction was selected, including AREG, FOSL2, ANKRD1, NCAM1, TNFRSF12A, LDLR, HMGCS1, INSIG1, IDI1, SQLE, FDFT1, SREBF2, MVD, and GGPS1. Gene expression levels for these selected genes were averaged across disease stages using the AverageExpression() function, and the data were log transformed. A heatmap was then generated to visualize the gene expression patterns across different disease stages after scaling the data.

QUANTIFICATION AND STATISTICAL ANALYSIS

All statistical analyses were performed using GraphPad Prism 10. The association of a normally distributed variable between two groups of interest was assessed using Student's *t* test. When more than 2 groups were considered, a one-way ANOVA was used to check for statistical association. Lastly, a two-way ANOVA was conducted to examine the influence of two independent variables on a dependent variable. Dunnett's post-hoc test was used when one condition was taken as the control; otherwise, Tukey's test was applied.

Quantitative data are shown as mean ± standard deviation (SD). The number of biological replicates (n) is indicated in the figure legends for each experiment. Data are considered statistically significant when $p < 0.05$. In all figures, *p*-values are summarized as follows: n.s., not significant; $^{*}p < 0.05$; $^{**}p < 0.01$; $^{***}p < 0.001$.